HHS Public Access

Author manuscript

Nat Immunol. Author manuscript; available in PMC 2024 August 01.

Published in final edited form as:

Nat Immunol. 2024 February ; 25(2): 294–306. doi:10.1038/s41590-023-01720-w.

The transcriptional cofactor Tle3 reciprocally controls effector and central memory CD8+ T cell fates

Xin Zhao[1,2], **Wei Hu**[1,2], **Sung Rye Park**[1,2], **Shaoqi Zhu**[2,3], **Shengen Shawn Hu**[4], **Chongzhi Zang**[4,5], **Weiqun Peng**[3], **Qiang Shan**[7,8], **Hai-Hui Xue**[1,6,8]

[1]Center for Discovery and Innovation, Hackensack University Medical Center, Nutley, NJ 07110

[3]Department of Physics, The George Washington University, Washington DC, 20052

[4]Center for Public Health Genomics, University of Virginia School of Medicine, Charlottesville, VA, USA

[5]Department of Public Health Sciences, University of Virginia, Charlottesville, VA, USA

[6]New Jersey Veterans Affairs Health Care System, East Orange, NJ 07018

[7]National Key Laboratory of Immunity and Inflammation, Suzhou Institute of Systems Medicine, Chinese Academy of Medical Sciences & Peking Union Medical College, Suzhou, Jiangsu, China 215123

Abstract

CD62L$^+$ central memory CD8$^+$ T (T_{CM}) cells are derived from antigen-experienced cells and provide long-term protection against the same pathogen. In spite of the therapeutic importance, approaches to enhance T_{CM} production remain limited. Here we show genetic ablation of Tle3, a transcriptional cofactor, promotes T_{CM} cell formation in response to acute viral infection, at the expense of CD62L$^-$ effector memory CD8$^+$ T (T_{EM}) cells. Lineage-tracing studies demonstrate that Tle3-deficient T_{EM} and terminally differentiated cytotoxic effector T cells both effectively give rise to T_{CM} cells, and the converted T_{CM} cells retain robust recall capacity. Mechanistically, Tle3 is dynamically redistributed in the T cell genome during effector and memory CD8$^+$ T cell differentiation, integrating regulatory activities from distinct sets of partner transcriptional factors expressed at different stages. Consistent with its known corepressor function, Tle3 coopts Runx3 and Tcf1 to limit chromatin accessibility at T_{CM}-characteristic sites and restrain expression of T_{CM} signature genes. Unexpectedly, Tle3 acts as a coactivator for Tbet to directly increases chromatin opening at T_{EM}-characteristic sites and activates T_{EM} signature gene transcription. The dual regulatory functions indicate that Tle3 is a gatekeeper for T_{EM} lineage fidelity, and further suggest that manipulating the Tle3 pathway can reprogram the fate decision of antigen-experienced CD8$^+$ T cells to favor T_{CM} production.

[8]Corresponding authors: Hai-Hui Xue (Contact), 111 Ideation Way, Bldg. 102, Rm. A417, Nutley, NJ 07110, Tel: 201-880-3550; haihui.xue@hmh-cdi.org, Qiang Shan, 100 Chongwen Road, Suzhou Industrial Park, Jiangsu Province, P.R. China 215123, Tel: 0512-62875035. shanq2009@gmail.com.

[2]These authors contributed equally to this work.

Author contributions

X.Z., W.H., and Q.S. performed the experiments and analyzed the data; S.P., S.Z, and S.S.H. analyzed the NextGen sequencing data, with supervision from C.Z. and W.P.; H.-H.X. conceived and supervised the project, and wrote the paper with Q.S. All authors edited the paper.

CD8$^+$ T lymphocytes are essential players in mounting protective cellular immune responses against pathogens and malignantly transformed cells. A productive CD8$^+$ T cell response clears pathogens causing acute infections and forms memory CD8$^+$ T cells, which have heightened protective capacity and constitute the underlying basis for vaccines[1]. Memory CD8$^+$ T cells consist of heterogeneous subsets, with distinct distribution patterns and functionality[2, 3]. Compared with CD62L$^-$ effector memory CD8$^+$ T (T_{EM}) cells that are largely detected in circulation, CD62L$^+$ central memory CD8$^+$ T (T_{CM}) cells are more enriched in the secondary lymphoid organs, persist for longer duration and respond more robustly to rechallenge by the same pathogen[3, 4]. In term of developmental origin, T_{CM} cells are derived from multiple sources, including T_{EM} cells as an *in vivo* maturation process over time[5], and various effector subsets expressing higher levels of IL-7Rα, CD62L and/or Tcf1 within a time range from initial few divisions after CD8$^+$ T cell activation to the phase of fully differentiated cytotoxic effectors[6, 7, 8, 9, 10]. However, it remains an unaddressed question whether T_{EM} and effector subsets can be reprogrammed to expedite and/or enhance the production of T_{CM} cells so as to apply their superior functionality for translational use.

Differentiation of effector and memory CD8$^+$ T cells are instructed by a plethora of transcription factors (TFs)[11, 12]. The access to regulatory elements by sequence-specific TFs is controlled by their dynamic expression, for example, Tbet and Blimp1 are induced in effector and partly retained in memory CD8$^+$ T cells, while Tcf1 and Myb are downregulated in effector but partly restored in memory CD8$^+$ T cells[7, 13, 14, 15]. TFs do not act alone and require cofactors to achieve regulatory specificity, stability, and transcriptional output, and this is particularly important for TFs such as Runx3 which are stably expressed throughout CD8$^+$ T cell differentiation process[16, 17]. One of such cofactors, Transducin-Like Enhancer of split (Tle) protein, stands out because its interaction with many immune function-related transcription factors including Tcf1/Lef1, Runx1/Runx3, Myc and Blimp1[18, 19, 20, 21]. Tle proteins are the mammalian homologues of *Drosophila* Groucho transcriptional repressor. There are four mammalian Tle genes, *Tle1–4*, that encode full-length Tle proteins, and these Tle proteins have both unique and redundant functions in development of multiple organs, including hematopoiesis[22, 23, 24, 25]. In T lineage cells, *Tle3* is most abundantly expressed, followed by *Tle4* and *Tle1*, with *Tle2* at a barely detectable level [26]. *Tle1*, *Tle3*, and *Tle4* are critically required for CD8$^+$ T cell lineage choice during thymic development, in a gene-dose dependent manner[26]. In this study, we demonstrate that Tle3 is dynamically redistributed in the T-cell genome during effector and memory CD8$^+$ T cell differentiation and that genetic ablation of Tle3 endows T_{CM}-forming capacity to fully differentiated effector cells and promotes maturation of T_{EM} to T_{CM} cells in anti-pathogen and anti-tumor responses.

Results

Loss of Tle3 enhances T_{CM} cell formation on population and single cell levels.

Because of known functional redundancy among Tle proteins during thymic development[26], we crossed *Gzmb-Cre* with *Tle1*-, *Tle3*-, and *Tle4*-floxed alleles[26, 27, 28] to ablate these genes only after CD8$^+$ activation, without perturbing thymic maturation. We obtained *Gzmb-Cre*$^+$*Rosa26*^{GFP} *Tle1*$^{FL/FL}$ *Tle3*$^{FL/FL}$ *Tle4*$^{FL/FL}$ mice and *Gzmb-Cre*$^-$ littermate

controls (called *Tle134*$^{-/-}$ and WT, respectively), where *Rosa26*^{GFP} allele expresses GFP after Cre activation and hence marks *Tle1,3,4*-deleted cells. WT and *Tle134*$^{-/-}$ mice were infected with lymphocytic choriomeningitis virus (LCMV) Armstrong strain (LCMV-Arm) to elicit acute viral infection. On 8th day post-infection (*dpi*) when the activated CD8$^+$ T cells reached peak response, *Tle134*$^{-/-}$ mice showed greatly diminished frequency and numbers of effector CD8$^+$ T (T_{EFF}) cells, detected as CD11a^{hi}CD8^{lo} poly-clonal antigen-experienced cells or LCMV GP33 epitope-specific cells measured with GP33-tetramer or GP33 peptide-stimulated IFN-γ production (Fig. 1a). This catastrophic impact on T_{EFF} cells by Tle1,3,4 deficiency was more profound than that by ablating Runx3, Tbet or Blimp1 alone[7, 13, 17, 29], consistent with the ability of Tle cofactors to interact with and integrate actions of multiple sequence-specific TFs.

In spite of the strong redundancy among Tle proteins in accumulation of T_{EFF} cells, we hypothesized that an individual Tle protein could finetune select functional aspects of CD8$^+$ T cell responses that cannot be fully compensated by its coexpressed homologues, similar to a more dominant effect of Tcf1 among the Tcf/Lef family TFs in T lineage cells[20, 30]. We focused on Tle3 because of its abundant expression in both naive CD8$^+$ (T_N) and T_{EFF} cells (Fig. 1b), and generated P14$^+$ *Gzmb-Cre*$^+$*Rosa26*^{GFP} Tle3$^{FL/FL}$ (*Tle3*$^{-/-}$) and *Tle3*$^{+/+}$ control (WT) mice, where the transgenic P14 TCR is specific for the GP33 epitope in LCMV. CD45.2$^+$WT or *Tle3*$^{-/-}$ P14 T_N cells were adoptively transferred, followed by LCMV-Arm infection (Fig. 1c). On 8 *dpi*, loss of Tle3 reduced the expansion of P14 CD8$^+$ T cells by ~3.5-fold (Fig. 1d), modestly reduced IFN-γ production, but showed little effect on TNF production and granzyme B expression (Extended data Fig. 1a–c). Additionally, the composition of KLRG1^{hi}IL-7Rα$^-$ fully differentiated T_{EFF} and KLRG1^{lo}IL-7Rα$^+$ memory precursor (T_{MP}) cells was similar between *Tle3*$^{-/-}$ and WT P14 cells (Fig. 1e). At ≥30 *dpi*, similar numbers of WT and *Tle3*$^{-/-}$ memory CD8$^+$ T (T_M) cells were detected (Fig. 1d), which might be partly ascribed to a modest reduction of Annexin-V$^+$ *Tle3*$^{-/-}$ compared to WT cells during the contraction phase (*e.g.*, 14 *dpi*, Fig. 1f). Interestingly, the CD62L$^+$ T_{CM} cell frequency and numbers were substantially elevated in the absence of Tle3 (Fig. 1g), while *Tle3*$^{-/-}$ T_{CM} and T_{EM} cells showed similar capacity of multi-cytokine production, but modestly reduced granzyme B expression compared with their WT counterparts (Fig. 1h,i). In this experimental setting, wild-type B6 mice were used as recipients, and the endogenous immune response should be sufficient to clear LCMV. To ascertain that the phenotypic changes in *Tle3*$^{-/-}$ T_M cells were not due to persistence of viral antigens, sera were collected from recipient mice at various time points. As determined with quantitative RT-PCR and plaque assays, LCMV was detected at similar levels in recipients of WT and *Tle3*$^{-/-}$ P14 cells on 4 *dpi*, but was below detection limits on 8, 14, and 30 *dpi* (Extended data Fig. 1d–f). We next performed co-transfer of CD45.2$^+$ *Tle3*$^{-/-}$ and CD45.1$^+$CD45.2$^+$ WT P14 cells into the same CD45.1$^+$ recipients followed by LCMV-Arm infection so that they would be exposed to the same *in vivo* environment. At ≥30 *dpi*, *Tle3*$^{-/-}$ T_M cells exhibited elevated T_{CM} frequency compared to WT cells (Extended data Fig. 1g), suggesting that Tle3-deficient cells had intrinsic propensity of favoring T_{CM} formation. These functional analyses collectively demonstrate that Tle3 supports T_{EM} fate and targeting Tle3 instead promotes T_{CM} formation. It is of note that targeting known Tle partner TFs shows distinct effects, *e.g.*, ablating Runx3 diminishes T_{MP} frequency at the effector phase, while ablating

Tcf1 impairs T_{CM} formation at the memory phase[15, 31]. Therefore, the impact of Tle3 deficiency is not a phenocopy of ablating a single partner TF. We posit that Tle3 has unique regulatory functions in memory $CD8^+$ T cell differentiation by engaging different TF complexes, and its distinct impact is ascribed to integrative effect of TF complexes that are uniquely sensitive to loss of Tle3 and cannot be compensated by Tle1 and Tle4.

To substantiate the unique function of Tle3 in promoting T_{EM} cell fate without depending on a single CD62L marker, we performed single-cell RNA sequencing (scRNA-seq) on WT and *Tle3*$^{-/-}$ P14 T_M cells sort-purified at ≥30 *dpi*. Focused analysis of WT T_M cells identified three major populations besides a minor population of few cells showing elevated expression of *Dock2*, which is reportedly associated with pool size of "virtual memory" T cells[32] (Fig. 2a,b). Further analysis of population signature genes revealed that one population was highly enriched with T_{CM}-characteristic genes including *Sell* (encoding CD62L), *Ccr7*, *Il7r* and *Tcf7* (encoding Tcf1) (Fig. 2c top row), and hence termed T_{CM} population (Fig. 2a). The other two populations expressed higher levels of T_{EM} characteristic genes including *Klrg1*, *Cx3cr1*, *Zeb2* and *Bhlhe40*, and termed $T_{EM}1$ and $T_{EM}2$ populations, with the later expressing a distinctively higher level of *Klre1* (Fig. 2b, and 2c bottom row). Pseudotime trajectory analysis with Monocle[33] suggested maturation of $T_{EM}2$ to $T_{EM}1$ and T_{CM} cells (Fig. 2d), consistent with existing knowledge[5]. When combined together, WT and *Tle3*$^{-/-}$ T_M single cells were resolved into 7 clusters, with Cluster 7 being equivalent to *Dock2*-hi population described above (Fig. 2e). Among the other 6 major clusters, WT and *Tle3*$^{-/-}$ T_M cells were distributed in almost exclusive clusters (Fig. 2f), suggesting a strong transcriptomic diversification due to Tle3 deficiency. Clusters 1–3 were mostly WT T_M cells (Fig. 2g), with cluster 3 being equivalent to WT T_{CM} cells based on characteristic gene expression (Fig. 2h). On the other hand, Clusters 4–6 were predominantly *Tle3*$^{-/-}$ T_M cells, where cluster 4 expressed higher levels of T_{EM}-characteristic genes, while clusters 5 and 6 strongly expressed T_{CM}-characteristic genes (Fig. 2g,h). Based on comparison between T_{CM} and $T_{EM}1/2$ clusters in WT cells, we defined single cell-based T_{CM} and T_{EM} signature genes (Extended Data Fig. 2a, Table S1). By assessing collective behavior of the signature gene sets, the WT-predominant Cluster 3 and *Tle3*$^{-/-}$-predominant Clusters 5 and 6 were enriched in T_{CM} scores but depleted of T_{EM} scores (Extended Data Fig. 2b,c). These single cell-based analyses indicate that targeting Tle3 facilitates acquisition of T_{CM} cell features on the single cell level, beyond a sole surface marker.

Tle3 promotes T_{EM} but suppresses T_{CM} molecular features

Consistent with previous studies[3, 34, 35], our scRNA-seq analysis of T_M cells showed that *Klrg1* and *Cx3cr1* transcripts were preferentially detected in WT T_{EM} over WT T_{CM} cells (Fig. 2b,c). While these features were retained in *Tle3*$^{-/-}$ T_M cells, their transcript levels appeared to be lower in *Tle3*$^{-/-}$ T_{EM} cells compared with their WT counterparts (compared cluster 4 with clusters 1 and 2 in Fig. 2h). These transcript changes were validated on protein levels (Extended data Fig. 3a), suggesting that Tle3 may be directly involved in regulating the expression of these genes (also see below, Fig. 4f in particular). Thus, the varied changes in marker protein expression due to Tle3 deficiency may not accurately reflect composition changes in T_M cell pool. Based on these considerations, we chose to use CD62L-based, classical definition of T_{EM} and T_{CM} cells (sorting strategy in Extended data Fig. 3b) for

multiomics-based mechanistic studies, so as to avoid potentially confounding effect caused by differential dependence of selected cell surface markers on Tle3. We first performed bulk RNA-seq analysis of WT and *Tle3*$^{-/-}$ T_{CM} and T_{EM} cells sort-purified at ≥30 *dpi* to increase transcript sequencing depth. Each cell type was in distinct clusters on principal component analysis (PCA) (Fig. 3a). Comparison between WT T_{CM} and WT T_{EM} cells identified 181 T_{CM} signature genes, including *Id3*, *Eomes*, *Irf8* and *Vcam1* (which were not captured by scRNA-seq), in additional to *Sell*, *Ccr7*, *Il7r* and *Tcf7*, and 90 T_{EM} signature genes such as *Cx3cr1* and *Klrg1* (Fig. 3b, Table S2). Combined with differentially expressed genes (DEGs) between WT *vs.* *Tle3*$^{-/-}$ T_{CM} and those between WT *vs.* *Tle3*$^{-/-}$ T_{EM} cells (Extended data Fig. 3c,d), the 1,272 DEGs were resolved into 5 expression clusters (ExpC1–5, Fig. 3c) by unsupervised K-means clustering analysis. Consistent with the known corepressor function of Tle3, ExpC1 and ExpC2 genes showed concordant increase in *Tle3*$^{-/-}$ T_{CM} and T_{EM} cells (defined as "Tle3-repressed genes"), with ExpC2 genes being more enriched in T_{CM} signature genes and showing more evident induction in *Tle3*$^{-/-}$ T_{EM} cells (Fig. 3c). On the other hand, loss of Tle3 caused downregulation of a large number of genes as distributed in ExpC3–5 (defined as "Tle3-actived genes"), with ExpC5 genes being more enriched with T_{EM} signature genes (Fig. 3c). Gene set enrichment analysis (GSEA) further demonstrated that *Tle3*$^{-/-}$ T_{EM} cells were depleted of T_{EM} signature genes but were strongly enriched in T_{CM} signature genes (Fig. 3d,e). As validated on protein levels, IL-7Rα, Tcf1 and Eomes were expressed at higher levels in WT T_{CM} than WT T_{EM} cells, and showed more pronounced induction in *Tle3*$^{-/-}$ T_{EM} cells (Fig. 3f). The T_{EM}-characteristic KLRG1 and CX3CR1 proteins showed reduced expression in *Tle3*$^{-/-}$ cells, especially T_{EM} cells (Fig. 3g), suggesting a positive regulatory role by Tle3. The transcriptomic analyses thus suggest that Tle3 exerts dual functions, *i.e.*, promoting T_{EM} but suppressing T_{CM} transcriptional program.

We next used ATAC-seq to examine the chromatin accessibility (ChrAcc) profiles in WT and *Tle3*$^{-/-}$ T_{CM} and T_{EM} cells. WT T_{CM} and WT T_{EM} cells were in distinct clusters based on PCA, and a direct comparison identified 1,881 T_{CM} and 2,643 T_{EM} signature ChrAcc sites (Fig. 4a,b). *Tle3*$^{-/-}$ T_{CM} and T_{EM} cells tended to cluster together and close to WT T_{CM} cells on the PCA, and showed strong diversification from their WT counterparts (Fig. 4a). A total of 5,553 differential ChrAcc sites between WT and *Tle3*$^{-/-}$ cells were resolved into 8 clusters with K-means (Fig. 4c, Extended data Fig. 3e). ChrAcc sites in clusters 1–5 showed concordant increase in *Tle3*$^{-/-}$ T_{CM} and T_{EM} cells (defined as "Tle3-closed sites"), and those in clusters 4 and 5 exhibited high frequency overlap with T_{CM} signature sites (Fig. 4c); on the other hand, clusters 6–8 sites showed decreased ChrAcc in *Tle3*$^{-/-}$ T_{CM} and T_{EM} cells (defined as "Tle3-opened sites"), and the decrease was most pronounced in cluster 6, with high-frequency overlap with T_{EM} signature sites (Fig. 4c). These analyses together demonstrate that Tle3 promotes T_{EM} but suppresses T_{CM} ChrAcc landscape, in line with its dual impact on T_{EM}/T_{CM} transcriptomes.

Tle3 is dynamically redistributed during CD8$^+$ T cell responses

To discern if Tle3 executes its dual functions in direct or indirect manner, we used CUT&RUN[36] to map genome-wide Tle3 binding sites in sort-purified T_N, T_{EFF} (8 *dpi*), T_{EM} and T_{CM} cells (at ≥30 *dpi*). PCA showed that Tle3 binding in these cell types

reproducibly formed distinct clusters (Extended data Fig. 4a). A total of 34,292 Tle3 binding sites were identified in all 4 cell types using MACS2[37]. By applying stringent criteria (≥3 fold difference in binding strength and FDR<0.05) in DEseq2[38], 3,627 Tle3 binding sites exhibited significant gain or loss in binding strength in T_{EFF}, T_{EM} and T_{CM} compared with T_N cells, and were distributed into 3 major clusters (Fig. 4d, Extended data Fig. 4b). Cluster1 showed little Tle3 binding in T_N, but acquired strong binding in T_{EFF}, and inherited into T_{EM} cells as well T_{CM} cells to a lesser extent (as in TleC1a-d subclusters, Fig. 4d). The Cluster1 Tle3 binding sites, defined as "T_{EFF}-acquired sites", were linked to genes in "immune system processes" as determined with GREAT analysis[39] (Extended data Fig. 4c); specifically, these sites were associated with genes in the cytotoxic program, as observed at upstream of *Tbx21* and *Ifng* genes (encoding Tbet TF and IFN-γ, Extended data Fig. 4d). Cluster2 Tle3 binding sites were similar as Cluster1 but showed stronger binding in T_{EM} and/or T_{CM} cells (defined as "T_M-preferred sites"), as exemplified in *Tbx21* introns (Extended data Fig. 4d). In contrast, Cluster3 Tle3 binding sites were strong in T_N but reduced in T_{EFF}, and hence defined as "T_{EFF}-attenuated sites" (as in TleC3a-e subclusters, Fig. 4d). The Cluster3 sites mostly remained weak in T_{EM}, but those in C3b,c,d subclusters partly restored Tle3 binding strength in T_{CM} cells (*i.e.*, stronger than T_{EFF}, remaining weaker than T_N cells) (Fig. 4d). The Cluster3 sites were linked to genes in "immune system processes" (Extended data Fig. 4e), especially memory-characteristic genes, such as *Ccr7* and *Zeb1* (Extended data Fig. 4f)[40]. We then examined Tle3 binding events within the +/–100kb regions flanking transcription start sites (TSSs) of DEGs between WT and *Tle3*$^{-/-}$ T_M cells. Approximately 40% of Tle3-repressed genes in ExpC1–3 harbored these dynamic Tle3 binding sites, and significantly, over 60% of Tle3-activated genes in ExpC5 (enriched in T_{EM} signature genes) were associated with dynamic Tle3 binding (Extended data Fig. 4g). The DEG-associated, dynamic Tle3 binding sites were mostly distributed in distal regulatory regions (Extended data Fig. 4h). These data suggest that Tle3 is actively redeployed in the T cell genome to meet functional needs during $CD8^+$ T cell differentiation.

We then stratified the dynamic Tle3 binding clusters (Fig. 4d) with differential ChrAcc clusters (Fig. 4c). Strikingly, Tle3-opened chromatin sites in ChrAccC6–7 were highly enriched with "T_{EFF}-acquired" Tle3 binding sites (TleC1a-d), and to a lesser extent with "T_M-preferred" sites (TleC2a-b) (Fig. 4e, red rectangle). As observed at the T_{EM} signature genes, such as *Klrg1*, *Cx3cr1*, *Prdm1*, and *Bhlhe40*, Tle3 acquired *de novo* binding sites in T_{EFF} and T_{EM} cells, which showed much more potent signals than T_{CM} cells at the same genomic locations (Fig. 4f, upper panels); and importantly, intact expression of Tle3 was necessary for keeping these Tle3 binding sites in open chromatin state in T_{EM} as well as T_{CM} cells (Fig. 4f, lower panels). Additionally, T_{CM} and T_{EM} cells had ~20,000 Tle3 binding sites that showed <3-fold differences in binding strength compared with T_N cells. These "less dynamic" Tle3 binding sites overlapped more frequently with Tle3-opened ChrAccC6–8 sites than with Tle3-closed ChrAccC1–5 sites (Extended data Fig. 5a). These observations suggest that Tle3 directly contributes to establishing and/or maintaining chromatin open state, especially at genes associated with the T_{EM} program.

Tle3 engages distinct TF partners during CD8$^+$ T cell responses

We next investigated how Tle3 achieved positive control of ChrAcc. *De novo* motif analysis with HOMER[41] showed that the "T_{EFF}-acquired" Tle3-bound, Tle3-opened ChrAcc sites (in red rectangle in Fig. 4e) were enriched in Ets, Runx and Tbet motifs (Fig. 5a) and that the "less dynamic" Tle3-bound, ChrAccC6–8 sites also had Ets, Runx and Tbet as top motifs (Extended data Fig. 5b), suggesting that Tle3 engaged both stably expressed Runx3 and T_{EFF}-induced Tbet to sustain chromatin open state during T_{EM} differentiation. It is well-documented that Tle cofactors interact with Runx family TFs[42, 43], but it is unknown if Tle3 engages Tbet. By immunoprecipitation with an anti-FLAG antibody, the FLAG-tagged Tbet was coimmunoprecipitated with HA-tagged Tle3 in 293T cells and endogenous Tle3 protein in primary T_{EFF} cells (8 *dpi*) (Fig. 5b,c), indicating physical interaction between Tle3 and Tbet. To further determine the cooperativity of Tle3 with Tbet and Runx3 TFs, we compared their binding patterns in T_{EFF} cells, because the "T_{EFF}-acquired" Tle3 binding sites largely sustained the binding strength in T_{EM} cells (Fig. 4d). By CUT&RUN analysis in T_{EFF} cells isolated on 8 *dpi*, we identified 15,498 Runx3 binding sites and 21,354 Tbet binding sites. Tle3 bound to 17,875 genomic locations in T_{EFF} cells, with 65% co-occupied by Runx3 and 81% co-occupied by Tbet, and significantly, Tle3 colocalized with both Runx3 and Tbet at 54% of its binding locations, suggesting formation of multipartite complexes (Fig. 5d). When focusing on "T_{EFF}-acquired" Tle3 binding sites (TleC1a-d) that gained binding strength in T_{EFF} and T_{EM} cells, Tle3 showed more prevalent colocalization with Tbet and Runx3, with ~88% sites exhibiting Tle3 and Tbet colocalization (Fig. 5e). These observations suggest that Tle3 functions as a cofactor Runx3 and T_{EFF}-induced Tbet for target gene regulation.

To further substantiate this point, we generated P14$^+$*hCD2-Cre*$^+$Rosa26^{GFP} *Tbx21*$^{FL/FL}$*Runx3*$^{FL/FL}$ mice (called *TRKO* herein)[44], used WT and *TRKO* P14 cells in adoptive transfer and LCMV-Arm infection (as in Fig. 1c), and then performed Tle3 CUT&RUN on early T_{EFF} cells isolated on 4 *dpi*. WT and *TRKO* T_{EFF} cells showed distinct Tle3 binding profiles (Extended data Fig. 5c), with over 3,000 Tle3 binding sites exhibiting diminished binding strength in *TRKO* compared to WT T_{EFF} cells (Fig. 5f). The Tbet/Runx3-dependent Tle3 binding sites were frequently observed at T_{EM}-characteristic genes, such as *Ifng*, *Gzmb*, *Klrg1* and *Prdm1* (Fig. 5g), with extensive overlap with Tbet and Runx3 binding sites, corroborating cooperativity of Tle3 with both Tbet and Runx3 TFs. To specifically assess Tbet for its contribution to Tle3 binding events, we also generated P14$^+$*hCD2-Cre*$^+$Rosa26^{GFP} *Tbx21*$^{FL/FL}$ mice (called *TbetKO* herein) and performed Tle3 CUT&RUN on WT or *TbetKO* early T_{EFF} cells as above. While 22,467 Tle3 binding sites were identified in WT T_{EFF} cells, only 13,393 Tle3 sites were found in *TbetKO* T_{EFF} cells (Extended data Fig. 5d), suggesting that Tle3 binding was substantially weakened in the absence of Tbet. In fact, the 9,926 Tle3 sites that were only identified in WT cells showed pronounced reduction in binding strength in *TbetKO* T_{EFF} cells, whereas the 731 Tle3 sites uniquely identified in *TbetKO* T_{EFF} cells had stronger binding strength than WT cells (Extended data Fig. 5e). The 3,380 Tbet/Runx3-dependent Tle3 binding sites defined above exhibited collectively attenuated binding strength in *TbetKO* T_{EFF} cells (Extended data Fig. 5f). Specifically, Tle3 binding at the *Ifng*, *Gzmb*, and *Prdm1* gene loci showed consistently reduced binding strength in *TbetKO* T_{EFF} cells (Extended data Fig. 5g), albeit

at a modest level compared with that in *TRKO* T_{EFF} cells. Additionally, diminished Tle3 binding in *TbetKO* T_{EFF} cells was observed at other T_{EFF}-associated genes such as *Gzma*, *Cx3cr1* and *Irf4* (Extended data Fig. 5g). In aggregates, these data demonstrate that Tbet and Runx3 are both critical for Tle3 recruitment and its stabilized binding, and further suggest that Tle3 functions as an integrator of Tbet and Runx3 TFs to promote activation of T_{EFF} transcriptional program, and their cooperativity is inherited into T_{EM} cells to safeguard their lineage fidelity.

We next investigated the direct connection between Tle3-TF complexes and T_{EM} molecular features. Among the Tle3-opened ChrAccC6–8 sites, 1,211 sites were T_{EM} signature ChrAcc sites (Fig. 4c). Two hundreds and four of the T_{EM} signature sites overlapped with "T_{EFF}-acquired" Tle3 binding sites, with 54% co-occupied by Tbet and 41% by both Tbet and Runx3 (Fig. 5h), demonstrating that Tle3 functions as a critical cofactor for Tbet to establish/maintain the open state of T_{EM} signature sites. By examining +/–100kb regions flanking the TSS of DEGs, "T_{EFF}-acquired" Tle3-bound, Tle3-opened ChrAcc sites were predominantly associated with Tle3-activated genes (Fig. 5i, top). Focusing on DEGs between WT and *Tle3*$^{-/-}$ T_{EM} cells specifically, Tle3 deficiency resulted in concordant reduction in ChrAcc and gene expression (quadrant *iii* in Fig. 5j), as observed at the T_{EM} signature genes, such as *Klrg1*, *Cx3cr1*, *Prdm1*, and *Bhlhe40* (Fig. 4f). Significantly, several Tle3-activated T_{EM} signature genes required intact expression of Tbet and Runx3 for normal expression from the early T_{EFF} stage, with *Klrg1*, *Esm1*, and *S1pr5* showing clear dependence on Tbet (Fig. 5k), further corroborating that Tle3 engages both Tbet and Runx3 for establishing T_{EM} transcriptional program. Collectively, Tle3 acquired *de novo* binding sites in T_{EFF} and T_{EM} cells, and intact expression of Tle3 was necessary for keeping the Tle3 binding sites at open chromatin state and maintaining the expression of these T_{EM} signature genes.

On the flip side, Tle3-closed chromatin sites in ChrAccC1–5 showed much higher overlap frequency with "T_{EFF}-attenuated" Tle3 binding sites in Cluster3 than that with "T_{EFF}-acquired" sites in Cluster1 (Fig. 4e, blue square), and these sites were enriched in Runx and Tcf/Lef motifs beside the Ets motifs (Extended data Fig. 6a). By focusing on the 692 T_{CM} signature ChrAcc sites that became more open in *Tle3*$^{-/-}$ T_M cells (in Tle3-closed ChrAccC1–5, Fig. 4c), 127 sites overlapped with "T_{EFF}-attenuated" Tle3 binding sites, with 95% being preoccupied by Tcf1 in T_N cells based on our previously published Tcf1 ChIPseq data[45, 46], while 28% being co-occupied by Runx3 in T_{EFF} cells (Extended data Fig. 6b). Based on these observations, we posited that Tle3-closed T_{CM} signature ChrAcc sites might involve at least two non-exclusive mechanisms. The first required direct repression by Tle3-Runx3 complex, as observed at downstream regions of *Ccr7* and an intronic region of *Itgae* (encoding CD103, a marker for resident memory $CD8^+$ T cells) (Extended data Fig. 6c), where Tle3 binding was weakened in T_{EM} compared to T_N cells, but was nonetheless necessary to restrain ChrAcc. The second mechanism was likely secondary to elevated Tcf1 expression in *Tle3*$^{-/-}$ T_{EM} and T_{CM} cells (Fig. 3f). Tcf1 is highly expressed in T_N cells, but profoundly downregulated in T_{EFF} cells[47]. The attenuation of Tle3 binding in T_{EFF} cells can be partly ascribed to downregulation of its partner TF, Tcf1. The prevalent pre-occupancy by Tcf1 at the T_{CM} signature ChrAcc sites in T_N cells suggests that these sites were intrinsically accessible by Tcf1 and became more open when Tcf1 became more available

in *Tle3*$^{-/-}$ T_{EM} and T_{CM} cells. This was observed at the TSS and upstream regions of *Ccr7*, where multiple T_{CM} signature ChrAcc sites were co-occupied by the Tle3-Tcf1 complex in WT T_N cells. These mechanisms were evidently in play at the T_{CM}-characteristic genes, such as *Tcf7*, *Sell* and *Id3* (Extended data Fig. 6d), where the associated T_{CM} signature ChrAcc sites were increased in the absence of Tle3, but did not meet the stringent ≥3-fold change requirements. Collectively, these data support the notion that Tle3 restrained the expression of T_{CM}-characteristic genes in T_{EM} cells *via* direct and indirect mechanisms. Additionally, we also noted that the Tle3-closed ChrAcc sites overlapping with "T_{EFF}-attenuated" Tle3 binding sites showed similar rate of association with Tle3-repressed and Tle3-activated genes (Fig. 5i, quadrant *i* and *iv* in Fig. 5j, respectively), suggesting that Tle3-repressed elements could function as enhancers or silencers depending on the gene context. In the *Il2ra* gene for example, the increased ChrAcc sites in *Tle3*$^{-/-}$ T_{EM} cells might be potential silencers, leading to diminished CD25 expression (Extended data Fig. 6e). These analyses demonstrate that the combinatorial use of Tle3-mediated activating and repressive functions favors T_{EM} but restrains T_{CM} formation process.

Targeting Tle3 reprograms memory CD8$^+$ T cell fate.

Given the Tle3 binding dynamics and its profound impact on ChrAcc and transcription states, we performed lineage tracing studies to determine its regulatory roles in fate decision and plasticity of memory CD8$^+$ T cells. Firstly, T_{EM} cells are known to convert to T_{CM} cells over time[5, 10]. On 14 *dpi* during CD8$^+$ T cell response to LCMV-Arm, the contraction of T_{EFF} cells largely concludes, with T_{EM} and T_{CM} cells starting to emerge. We sorted the 'emerging' WT or *Tle3*$^{-/-}$ T_{CM} and T_{EM} cells and transferred the same numbers of cells into infection-matched CD45.1$^+$ recipients. Twenty days later, both WT and *Tle3*$^{-/-}$ T_{CM} cells persisted as CD62L^{hi} cells, consistent with known T_{CM} lineage stability (Fig. 6a). In line with previous reports, ~1/4 of WT T_{EM} cells became CD62L^{hi}, while about half of *Tle3*$^{-/-}$ T_{EM} cells adopted CD62L^{hi} phenotype (Fig. 6a), suggesting that conversion/maturation of T_{EM} to T_{CM} cells was accelerated in the absence of Tle3. To further substantiate this point, we also sorted and transferred the 'established' WT or *Tle3*$^{-/-}$ T_{EM} cells at ≥30 *dpi* as above, and observed that *Tle3*$^{-/-}$ T_{EM} cells consistently gave rise to higher frequency of CD62L^{hi} cells than WT T_{EM} cells after 20 days (Fig. 6b).

Tle3 deficiency did not affect the T_{EFF} and T_{MP} composition on 8 *dpi* (Fig. 1e). To determine if loss of Tle3 caused intrinsic bias for T_{EM} vs. T_{CM} fate at this early stage, T_{EFF} and T_{MP} cells were sorted based on their characteristic KLRG1 and IL-7Rα expression patterns, and transferred into infection-matched recipients (Fig. 6c). Consistent with existing knowledge, WT T_{MP} cells gave rise to CD62L^{hi} cells after fifteen days, whereas WT T_{EFF} cells contributed little (Fig. 6c). Significantly, *Tle3*$^{-/-}$ T_{MP} and T_{EFF} cells both yielded CD62L^{hi} cells, with *Tle3*$^{-/-}$ T_{MP} cells showing higher efficiency (Fig. 6c). These data suggested that targeting Tle3 endows T_{CM}-producing capacity to the 'trerminally differentiated' T_{EFF} cells, in addition to accelerating T_{MP} to T_{CM} transition.

Because *Gzmb-Cre*-mediated target gene ablation occurs right after CD8$^+$ T cell activation even before the first division[48], the early deletion of Tle3 may have predetermined the T_{MP} vs. T_{EFF} fate decisions[8]. To investigate if Tle3 had continued roles in directing T_{MP} vs. T_{EFF}

differentiation, we generated P14^{+}CreER^{+} *Tle3*$^{FL/FL}$ and corresponding *Tle3*$^{+/+}$ littermate controls, and performed adoptive transfer of P14 CD8^{+} T cells coupled with LCMV-Arm infection (Fig. 6d). The recipients were treated on 6 and 7 *dpi* after T_{MP} vs. T_{EFF} fate decision was made and again on 21 *dpi* to ensure *Tle3* ablation. Two weeks later, analysis of T_M composition showed elevated T_{CM} frequency and numbers in P14^{+}CreER^{+} *Tle3*$^{FL/FL}$-derived T_M (called *Tle3*$^{\Delta CreER}$ herein) cells (Fig. 6e). In addition, induced deletion of Tle3 increased the expression of T_{CM}-characteristic Tcf1 and Eomes but reduced that of T_{EM}-characteristic CX3CR1 and KLRG1 in T_{EM} cells, without affecting their capacity of IFN-γ and TNF production (Extended data Fig. 7a–c). These data support a continuous requirement for Tle3 to restrain T_{CM} cell formation.

To investigate the impact of acute Tle3 deletion on 'established' T_M cells, CreER^{+} *Tle3*$^{FL/FL}$ or *Tle3*$^{+/+}$ P14 cells were adoptively transferred, recipients infected with LCMV-Arm as above. At ≥30 *dpi*, T_{EM} cells were sorted from the immune mice and cultured *ex vivo* with 4-hydroxy-tamoxifen (4-OHT) for 48 hrs, and the resulting *Tle3*$^{\Delta CreER}$ and WT T_{EM} cells were subjected to RNA-seq and ATAC-seq analyses (Extended data Fig. 8a, top path). A total of 171 DEGs was identified, with *Tle3*$^{\Delta CreER}$ T_{EM} cells showing reduced expression of T_{EM} signature genes such as *Klrg1*, *Gzma*, *Klra9* and *Ckb*, but increased expression of T_{CM} signature genes including *Sell*, *Ccr7*, *Eomes* and *Mapk11* (Fig. 7a). By GSEA without a preset cut-off, T_{EM} signature gene set was depleted, while T_{CM} signature gene set was enriched in *Tle3*$^{\Delta CreER}$ compared to WT T_{EM} cells (Fig. 7b,c). Because of the short-duration of induced Tle3 deficiency, the criteria of ≥1.5-fold changes and FDR<0.05 were adopted for ChrAcc profile comparison, 1,458 ChrAcc sites were more 'open', while 455 sites were more 'closed' in *Tle3*$^{\Delta CreER}$ compared to WT T_{EM} cells (Fig. 7d). Approximately 12% of these differential ChrAcc sites overlapped with T_M signature sites (as defined in Fig. 4b), and among these T_M signature-overlapping sites, the more 'closed' ChrAcc sites in *Tle3*$^{\Delta CreER}$ T_{EM} cells were enriched with T_{EM} signature sites, and the more 'open' ChrAcc sites in *Tle3*$^{\Delta CreER}$ T_{EM} cells were enriched with T_{CM} signature sites (Fig. 7e). Specifically, the more 'closed' ChrAcc sites in *Tle3*$^{\Delta CreER}$ T_{EM} cells were found at T_{EM} signature genes such as *Ckb* and *Klra9*, and effector function-associated genes including *Ifng* and *Bhlhe40* (Fig. 7f, top); on the other hand, the more 'open' ChrAcc sites in *Tle3*$^{\Delta CreER}$ T_{EM} cells were observed at T_{CM} signature genes including *Ccr7*, *Sell* and *Socs1* (Fig. 7f, bottom). These observations demonstrate that acute deletion of Tle3 had immediate impact on diminishing T_{EM} but promoting T_{CM} molecular features in T_{EM} cells, suggesting an early onset of T_{EM} to T_{CM} cell fate reprogramming upon loss of Tle3.

To validate such impact *in vivo*, the immune mice were treated with tamoxifen for two consecutive days, and on the third day (48 hrs after the initial tamoxifen treatment), T_{EM} cells were sorted and transferred into infection-matched recipients (Extended data Fig. 8a, middle path). After two weeks, *Tle3*$^{\Delta CreER}$ T_{EM} cells gave rise to higher frequency and numbers of CD62L^{+} cells than WT T_{EM} cells (Fig. 7g). To determine the functionality of Tle3-deficient T_{CM} cells, the immune mice were treated with tamoxifen but given two weeks to facilitate *in situ* "T_{EM}-to-T_{CM} reprogramming". The resulting T_{CM} cells were then sort-purified and transferred into *Rag1*$^{-/-}$ mice followed by infection with *Listeria monocytogenes* expressing the GP33 epitope (LM-GP33) (Extended data Fig. 8a, bottom path). In response to the recall stimulation, both WT and *Tle3*$^{\Delta CreER}$ T_{CM} cells underwent

expansion and generated similar numbers of secondary effector $CD8^+$ T cells (Fig. 7h), which showed similar capacity of IFN-γ production and granzyme B expression (Fig. 7i,j). While *Listeria* expanded rapidly in *Rag1*$^{-/-}$ mice due to lack of endogenous immune responses, the transfer of WT or *Tle3*$^{\Delta CreER}$ T_{CM} cells curbed bacterial expansion with similar efficacy (Fig. 7k), suggesting that T_{CM} functions were not detectably affected by loss of Tle3. To further corroborate this point, we tested the pathogen-experienced T_M cells in tumor control, with direct comparison with T_N cells. We utilized *Tle3*$^{\Delta CreER}$ T_M cells where *Tle3* was inducibly deleted at the effector phase (Fig. 6d), and transferred the same number of sort-purified $P14^+$ T_N, T_{CM} and T_{EM} cells into CD45-disparate recipients, followed by subcutaneous inoculation of B16 melanoma cells expressing the LCMV GP33 epitope (B16-GP33)[49, 50]. While all recipients of WT T_N cells succumbed by 21 days after inoculation due to uncontrolled tumor growth, the recipients of WT T_{EM} and WT T_{CM} cells showed improved survival and impeded tumor growth, with WT T_{CM} cells exhibiting stronger anti-tumor effect (Extended data Fig. 8b), consistent with previous reports[51, 52]. When Tle3-deficient T_M cells were transferred, the recipients of WT and *Tle3*$^{\Delta CreER}$ T_{EM} cells had similar kinetics of tumor growth, and those of *Tle3*$^{\Delta CreER}$ T_{CM} cells showed significantly slowed tumor growth than those of WT T_{CM} cells, albeit with similar survival curves (Extended data Fig. 8b,c). At the endpoint of the study (*i.e.*, day 33 after tumor inoculation) when only T_{CM} recipient mice survived, the recipients of *Tle3*$^{\Delta CreER}$ T_{CM} cells showed trends of reduced tumor sizes and increased numbers of tumor-infiltrating $CD8^+$ lymphocytes (TILs) compared to those of WT T_{CM} cells (Extended data Fig. 8d,e), whereas WT and *Tle3*$^{\Delta CreER}$ T_{CM}-derived TILs exhibited similar PD-1, Tim-3, and granzyme B expression (Extended data Fig. 8f,g). These data suggest that Tle3 ablation improved T_{CM} production without compromising their recall responses to pathogens or tumor antigens.

Discussion

It has been generally accepted that the terminally differentiated effector $CD8^+$ T cells have little contribution to T_{CM} formation, and T_{EM} cells undergo time-dependent, slow conversion to T_{CM} cells. Here we show that Tle3 functions a major gatekeeping factor that limits the plasticity of effector and T_{EM} cells. Ablating Tle3 endowed the T_{CM}-forming capacity to the terminally differentiated effector $CD8^+$ T cells, and greatly accelerated the conversion of T_{EM} to T_{CM} cells. Although the activated $CD8^+$ T cells may have intrinsic bias for effector vs. memory fate decision within the initial cell divisions[11, 53], our data demonstrate that such fate bias does not necessarily stay in fixation, but can be reprogrammed to favor T_{CM} production. Importantly, the converted T_{CM} cells mostly sustained their superior recall capacity in response to tumor antigen compared with naive $CD8^+$ T cells and even T_{EM} cells. These observations suggest that manipulating Tle3 expression and/or activity could be a useful strategy to improve anti-pathogen and anti-tumor immunity.

Sequence-specific TFs have been at the center of attention in regulating T cell development, differentiation and functions. Transcriptional coregulators, in spite of their unique capacity of interacting with multiple TFs, are largely left in neglect. The functional redundancy among the multiple Tle/Groucho cofactors has posed a unique challenge to dissecting their regulatory roles in T cell biology. Targeting all highly expressed Tle genes completely

crippled accumulation of antigen-specific effector $CD8^+$ T cells, a phenotype that was much more severe than targeting a single TF such as Runx3 or Tbet[7, 17, 31]. Such profound impact highlights the integrative functions of Tle cofactors from all TF complexes that utilize Tle proteins as a key component. On the other hand, selective targeting of Tle3 in this work demonstrated its unique requirement for sustaining T_{EM} cell pool while restraining T_{CM} formation. To our knowledge, this is a distinct function that has not been described for other TFs or epigenetic regulators. The biological impact of ablating Tle3 is likely a collective effect of perturbation of multiple TF complexes that are sensitive to reduction of Tle3 protein, which cannot be adequately compensated by the presence of co-expressed Tle1 and Tle4. In this sense, we propose that transcription coregulators including Tle/Groucho proteins should be considered in its own league, as integrators of TF complexes that are responsive to various external input.

Because of their ability to interact with multiple TFs, genomic distribution of Tle/Groucho proteins is expected to be dynamic, rather than static. Longitudinal tracking of Tle3 binding indeed revealed the dynamic redistribution of Tle3 in the $CD8^+$ T cell genome during effector differentiation and memory formation processes. The active gain of Tle3 binding in antigen-experienced T_{EFF}, T_{EM} and T_{CM} cells was concordant with induced Tbet expression in these cells. This study further identified Tbet as a new partner TF for Tle3, manifested in forms of physical protein-protein interaction and extensive colocalization in the T_{EFF} genome. The Tbet-Tle3 cooperativity frequently involves Runx3, a known partner of Tle/Groucho proteins, to form multipartite complexes, which might be achieved through recruitment of Tbet-Tle3 complex to Runx3 binding sites and/or Runx3-Tle3 complex to Tbet binding sites. In fact, intact expression of Tbet and Runx3 is critical for effective Tle3 recruitment and its stable engagement in the regulatory complexes. On the other end of the spectrum, Tle3 binding is attenuated in T_{EFF} and T_{EM} cells in another set of genomic locations, some of which partly restored Tle3 binding in T_{CM} cells. This Tle3 binding dynamics coincided with the expression pattern of Tcf1 and Lef1, classical TF partners for Tle cofactors, during $CD8^+$ T cell responses, and their colocalization was supported by enriched Tcf/Lef motifs and presence of Tcf1 ChIPseq peaks at these genomic locations. It is noteworthy that gain and attenuation of Tle3 binding both occurred at Runx3-bound genomic locations, indicating that Runx3 by itself is not a sole determinant for Tle3 recruitment. Additionally, the less restrictive “GGAA” Ets motif was highly enriched in “T_{EFF}-acquired” and “T_{EFF}-attenuated” Tle3 binding sites. Ets family TFs include more than 30 members and at least 10 of these were abundantly expressed in T lineage cells[54, 55]. Further investigations are required to dissect composition of TF-cofactor complexes during $CD8^+$ T cell responses, so as to fully understand Tle/Groucho dynamics. Nonetheless, our findings constitute an important step forward and highlight that Tle3 functions as an integrator of multiple transcriptional partners to regulate the plasticity of antigen-experienced $CD8^+$ T cells.

While Groucho and Tle proteins are historically known as transcriptional repressors[22, 24], their involvement in activating transcription has been observed in adipocytes[56, 57]. Our systematic molecular analyses revealed that Tle3 is responsible for ‘open’ chromatin state at its direct binding sites and is necessary for positive regulation of genes associated with such sites. In this capacity, the Tle3-Tbet complex appears to have a dominant role in activation of

T_{EM}-characteristic gene expression and chromatin accessibility landscape. In parallel, Tle3-dependent 'closed' chromatin state and gene repression contribute to restraining activation of T_{CM} program, where both Tle3-Runx3 and Tle3-Tcf1 complexes could act through direct and indirect mechanisms. The direct effect does not need to be prevalent in terms of the quantity of complex-occupied genomic locations, and a deregulation of a key downstream TF, such as Tcf1, could have profound impact. For example, genetic ablation of Runx3 in T_{EFF} cells caused aberrant activation of genes associated with follicular helper T (T_{FH}) cell program, giving rise to $Tcf1^{+}CXCR5^{+}$ cells with B-cell help function[17]. In this context, compound deletion of Tcf1 together with Runx3 did prevent the T_{FH} lineage divergence[17]. These findings reconcile nicely with the new observations in this work, which collectively indicate that Tle/Groucho-Runx3 complex, where all Tle proteins are likely involved, is responsible for complete repression of Tcf1 in T_{EFF} cells. Specific ablation of Tle3 and hence disruption of the Tle3-Runx3 complex resulted in more nuanced regulation of Tcf1, allowing modest activation of the T_{CM} program while avoiding the crippling effect of ablating Runx3 or all Tle proteins altogether on T_{EFF} and T_{M} cells[17, 31]. In sum, the combinatorial use of dual functions in gene regulation afforded Tle3 a unique capacity of guarding T_{EM} lineage fidelity, and releasing the Tle3 brake thus facilitates and accelerates formation of T_{CM} cells with better durability and more robust recall capacity.

METHODS

Mice.

C57BL/6J (B6), B6.SJL, $Rosa26^{GFP}$, *hCD2-Cre* transgenic, $Tbx21^{FL/FL}$ and $Runx3^{FL/FL}$ mice were from the Jackson Laboratory. $Tle3^{fl/fl}$, *Gzmb*-Cre transgenic, and Cre-ER knock-in mice were previously described[26, 58, 59]. All compound mouse strains used in this work were from in-house breeding at the animal care facilities of Hackensack University Medical Center. The mice were housed at 18–23°C with 40–60% humidity, with 12-hr light/12-hr dark cycles. All mice were 6–12 weeks of age, and both sexes were used without randomization or blinding. All mouse experiments were performed under protocols approved by the Institutional Animal Use and Care Committees of Center for Discovery and Innovation, Hackensack University Medical Center.

Flow cytometry.

Single-cell suspensions from the spleen and lymph nodes (LNs) were generated after mashing tissue through 70 μm cell strainer, and the cells were surface-, intracellularly or intranuclearly stained following standard protocols[50]. The fluorochrome-conjugated antibodies were as follows: anti-CD8 (53–6.7), anti-CD45.2 (104), anti-CD62L (MEL-14), anti-KLRG1 (2F1), anti-IL-7Rα (A7R34), anti-granzyme B (GB12), anti-IFN-γ (XMG1.2), anti-TNF (MP6-XT22), anti-IL-2 (JES6–5H4), and anti-Eomes (Dan11mag) were from Thermo Fisher Scientific. Anti-Tcf1 (C63D9) from Cell Signaling Technology; anti-CX3CR1 (SA011F11) from BioLegend. For detection of Eomes and Tcf1 proteins, surface-stained cells were fixed and permeabilized with the Foxp3/Transcription Factor Staining Buffer Set (eBiosciences/Thermo Fisher Scientific), followed by incubation with corresponding fluorochrome-conjugated antibodies. For cytokine staining, the cells were stimulated with GP33 (200 nM) in the presence of the protein transport inhibitor Brefeldin

A for 5 hrs at 37°C, followed by standard intracellular staining. For detection of cell survival status, the PE Annexin V Apoptosis Detection Kit (BD Biosciences) was used following the manufacturer's instruction. Cell sorting was performed on FACSAria (BD Biosciences). Data were collected on FACSCelesta flow cytometers (BD Biosciences) and were analyzed with FlowJo software v10.7.1 (TreeStar).

Adoptive transfer and acute infection.

Naïve P14 $CD8^+$ T cells were isolated from the lymph nodes of WT, *Gzmb-Cre*$^+$Rosa26^{GFP} *Tle3*$^{FL/FL}$ (*Tle3*$^{-/-}$), CreER$^+$ *Tle3*$^{FL/FL}$, *hCD2-Cre*$^+$Rosa26^{GFP} *Tbx21*$^{FL/FL}$ (*TbetKO*), or *hCD2-Cre*$^+$Rosa26^{GFP} *Tbx21*$^{FL/FL}$*Runx3*$^{FL/FL}$ (*TRKO*) P14 TCR transgenic mice, and adoptively transferred into $CD45.1^+$ B6.SJL recipients (2×10^4 cells/recipient). On the following day, the recipients were intraperitoneally (*i.p*) infected with 2×10^5 PFU of LCMV-Arm. Phenotypic, functional and molecular analyses were performed on 4 or 6 day post-infection (*dpi*) for early T_{EFF} phase, 8 *dpi* as T_{EFF} phase, and at 30–45 *dpi* as T_M phase. In lineage tracking studies, WT or *Tle3*$^{-/-}$ P14 $CD8^+$ T cells were first enriched from recipient spleens by depleting $CD45.1^+$ cells using EasySep Biotin Positive Selection Kit II (StemCell Technology). The enriched cells were then sorted for T_{EFF} and T_{MP} cells on 8 *dpi*, and for $CD62L^+$ and $CD62L^-$ cells on 14 or ≥30 *dpi*, and transferred into infection-matched $CD45.1^+$ B6.SJL recipients (1.5×10^6 T_{EFF}, 3×10^5 T_{MP}, 3×10^5 $CD62L^+$ or 5×10^5 $CD62L^-$ cells/recipient), which were analyzed after 14–20 days.

LCMV quantification.

Serum samples were collected from LCMV-Arm-infected mice at various timepoints, and the viral load was quantified with two complementary approaches. The first approach was quantitative PCR-based assay following a previously published protocol with minor adjustments[60]. In brief, total RNA was exacted from sera using TRIzol RNA isolation reagents, and reverse-transcribed with the Reverse Transcription Kit (Qiagen, RT31–100). The resulting cDNA was used as templates for quantitative PCR using the Universal SYBR Green Supermix (BioRad, Cat. No.1725271) and the following primers: 5'-CATTCACCTGGACTTTGTCAGACTC and 5'-GCAACTGCTGTGTTCCCGAAAC. The plasmid pHCMV-LCMV-Arm53b (Addgene, Cat. No. 15796) that expresses LCMV envelop glycoprotein[61] was used to establish a standard curve through 10-fold serial dilutions, and virus copy numbers were then calculated accordingly. The second approach was a function-based standard plaque formation assay[62]. In brief, VERO cells were incubated with serially diluted serum samples at 37°C with 5% CO_2 for 90 mins, and the cell monolayer was overlaid with 0.5% agarose dissolved in DMEM containing 5% FBS. Two days later, a layer of 0.02% neutral red was applied for overnight staining, and plaques were then counted.

T_{EM} characterization *ex vivo* and T_{CM} recall responses *in vivo*.

P14 Cre-ER$^+$ *Tle3*$^{+/+}$ or Cre-ER$^+$ *Tle3*$^{FL/FL}$ cells were adoptively transferred, and recipients were infected as above to establish immune mice. T_{EM} cells were sort-purified from the immune mice, cultured in the presence of 4-hydroxy-tamoxifen (4-OHT, 1 μM/ml), IL-7 and IL-15 (each at 10 ng/m) for 48 hrs, and viable WT and *Tle3*$^{\Delta CreER}$ cells were re-sorted for molecular characterization. At various timepoints (as illustrated in Fig. 6d and Extended data

Fig. 8a), the immune mice were administered with tamoxifen (4 mg/mouse) *via* oral gavage as previously described[30].

For eliciting recall response to acute infection, the resulting WT or *Tle3*$^{\Delta CreER}$ T_{CM} cells were sorted at 2 weeks after tamoxifen treatment and transferred into *Rag1*$^{-/-}$ mice (2×10^4 cells/recipient), followed by intravenous (*i.v.*) infection with LM-GP33 (5×10^6 CFUs/mouse). Three days, secondary effector $CD8^+$ T cells derived from T_{CM} cells were analyzed in the spleen, and bacterial burden was determined in the livers by colony formation assay as previously described[47].

To assess recall response in a tumor model, $P14^+$ T_N, WT or *Tle3*$^{\Delta CreER}$ T_{EM} or T_{CM} cells were sort-purified and transferred into naive B6.SJL mice (5×10^4 cells/mouse). One day later, the right flank of recipient mice was shaved, and subcutaneously (*s.c.*) injected with 2×10^5 B16 melanoma cells expressing the LCMV GP33 epitope (B16-GP33) as previously described[50]. The tumor size was monitored every other day from day 9 after tumor inoculation, when the tumor was palpable. Tumor progression was determined by measuring tumor length multiplied by width using an electronic digital caliper. Mice were euthanized when the tumor reached an animal protocol threshold including tumor area of ≥225 mm^2.

Immunoblotting and Immunoprecipitation.

To detect the abundance of Tle3 proteins, sorted naïve or effector CD8 T cells were extracted and immunoblotted with poly-clonal anti-Tle3 (Cat No.14464–1-AP, ProteinTech) and β-actin (13E5, Cell Signaling Technology). For detection of Tbet and Tle3 protein-protein interactions, FLAG-tagged Tbet and HA-tagged Tle3 cDNAs were subcloned into Mig-R1 plasmids and then co-transfected into 293T cells using Lipofectamine 2000 (Invitrogen/ThermoFisher Scientific). After 24 hrs, cell lysates were preincubated with ethidium bromide (EtBr, Bio-Rad Laboratories) at 100 μg/ml at 4°C for 30 min, followed by incubation with anti-FLAG antibody (clone M2, #F3165, MilliporeSigma) overnight at 4°C in the presence of EtBr and then 2-hr incubation with Dynabeads Protein G. The immunoprecipitated samples were immunoblotted with anti-HA (C29F4, Cell Signaling Technology). For detection of their interaction in murine primary effector $CD8^+$ T cells, P14 naive $CD8^+$ T cells were primed *ex vivo* and subjected to spinofection with retrovirus expressing FLAG-tagged Tbet and GFP, as previously described[17, 48]. The transduced $GFP^+CD45.2^+$ P14 cells were sort-purified and transferred into $CD45.1^+$ B6.SJL recipient mice, followed by LCMV-Arm infection. Six days later, $CD45.2^+$ donor-derived effector $CD8^+$ cells were enriched using EasySep PE positive selection kit (StemCell Technologies), the cell lysates were immunoprecipitated with the anti-FLAG antibody or IgG as above, followed by immunoblotting with the anti-Tle3 antibody.

Single cell RNA-seq (scRNA-seq) and data analysis.

WT or *Tle3*$^{-/-}$ P14 cells were adoptively transferred, and recipients were infected with LCMV-Arm as above. At 30–35 *dpi*, $CD45.2^+GFP^+$ P14 $CD8^+$ T cells were sort-purified, 5×10^3 live cells of each genotype were used to generate single-cell gel-bead in emulsion (GEM), and the scRNA-seq libraries were constructed with 10X Genomics Chromium

Next GEM Single Cell 5' library kit following the manufacturer's manual. The libraries were sequenced on Illumina's HiSeq4000 in paired-end read mode with the read length of 150 nucleotides at the Admera Health. The scRNA-seq data are deposited at the GEO (GSE216633) under the SuperSeries of GSE213041

Data processing and cell clustering.—Raw reads were processed following the instructions described in the Drop-seq Laboratory Protocol v3 using Drop-Seq Tools (v2.4.1) [63], and were aligned to mm10 mouse genome using STAR (v.2.7.9a) [64] following the default DropSeq-Tools pipeline. The aligned reads were further processed to generate digital gene expression files using Drop-Seq Tools (v2.4.1) [63], and unique molecular identifier (UMI) was calculated using Seurat (v4.1.2) [65]. Cells with UMI<1,000 and those with mitochondrial content higher than 2.5 were excluded for downstream analyses. The UMI counts in high quality cells were normalized to UMI count per million total counts and log-transformed. Variable genes were selected based on average expression and dispersion. Ten principal components based on variable genes were used for UMAP manifold learning and clustering analyses.

The clustering of WT memory $CD8^+$ T cells was performed using the shared nearest modularity optimization implemented in Seurat's *FindClusters* function with the resolution parameter as 0.5. Marker genes were identified with Seurat's *FindAllMarkers* function. Normalized gene expression data were shown as feature plots or violin plots, and scaled expression data of cluster marker genes were used to generate heatmaps. Trajectory analysis was performed using Monocle (v3) by learning a principal graph for the data and ordering cells along the graph [33], where the pseudotime scores of each cell are calculated from a full transcriptome profile using *pseudotime* function in Monocle. To define T_{CM} and T_{EM} signature genes based on single cell transcriptomes, the cells in $T_{EM}1$ and $T_{EM}2$ clusters were combined as T_{EM} cells and then compared with those in T_{CM} cluster. By criteria of ≥1.5 expression changes and FDR<0.05, 96 T_{CM} and 53 T_{EM} signature genes were identified.

For characterizing the impact of Tle3 deficiency, WT and *Tle3*$^{-/-}$ memory $CD8^+$ T cells were pooled for UMAP clustering analysis as above. Using T_{CM} and T_{EM} signature genes defined above, T_{CM} and T_{EM} scores were calculated for each cell using Seurat's "*AddModuleScore*" function. The T_{CM} and T_{EM} scores were mapped on UMAP clusters or as scatter plot for each cluster with ggplot2.

RNA-seq and data analysis.

WT or *Tle3*$^{-/-}$ P14 T_{CM} and T_{EM} cells were sorted from recipient mice at 30–35 *dpi*, and each cell type was collected in three biological replicates. *Ex vivo* cultured WT or *Tle3*$^{\Delta CreET}$ T_{EM} cells were re-sorted for viable cells and collected in three replicates as well. Total RNA was extracted with TRIzol RNA isolation reagents (Invitrogen/ThermoFisher Scientific), and used for RNA-seq library construction by Azenta Life Sciences. In brief, full-length cDNA synthesis was performed with SMART-Seq HT Ultra Low Input Kit (Clontech/Takara Bio), and then processed with Nextera XT DNA Library Kit (Illumina). The libraries were sequenced on Illumina HiSeq instruments (4000 or equivalent) in paired-

end read mode with the read length of 150 nucleotides. Raw sequence data (.bcl files) were converted into fastq files and de-multiplexed using the bcl2fastq 2.17 software (Illumina). The bulk RNA-seq data are deposited at the GEO (GSE213037 and GSE241532) under the SuperSeries of GSE213041.

The sequencing quality of RNA-seq libraries were assessed by FastQC (v0.11.9), and sequenced reads were then trimmed by 50 bp from the 3'-end to remove the low-quality bases using the Trimmomatic (v.0.39). The trimmed paired-end reads were mapped to the mm10 mouse genome using STAR-2.7.9a[64], and only the pairs with mapping quality (MAPQ) ≥ 30 and both ends mapped to the same chromosome were retained. The mapped reads were converted to gene expression matrix by featureCounts (v.2.0.1), and then processed with DESeq2 (v1.32.0)[38] to estimate expression levels of all genes as a gene-level Fragments Per Kilobase of transcripts per Million mapped reads (FPKM) values. Differentially expressed genes (DEGs) between a pair of conditions were identified by the criteria of ≥1.5-fold expression changes, FDR<0.05, and FPKM≥0.5 in the higher expression condition. DEGs from 3 key comparisons (defined in Extended data Fig. 3c) were collected for unsupervised K-means clustering analysis to define dynamic gene expression patterns.

Based on comparative analysis between WT T_{CM} and WT T_{EM} cell transcriptomes, T_{CM} and T_{EM} signatures were defined (Table S2) and used as custom gene sets in GSEA [66] to measure their relative enrichment in WT and Tle3-deficient T_{EM} cells.

CUT&RUN and data analysis.

Cleavage Under Targets and Release Using Nuclease (CUT&RUN) was used for genome-wide mapping of Tle3 binding sites in naïve WT $CD8^+$ T cells (3 biological replicates), WT T_{EFF} (8 *dpi*, 2 replicates), WT T_{EM} and T_{CM} cells (≥30 *dpi*, 2 biological replicates each), Tle3 binding sites in WT and Tbet/Runx3-deficient (*TRKO*) early T_{EFF} (4 *dpi*, 4 and 3 replicates, respectively), Tle3 binding sites in WT and Tbet-deficient (*TbetKO*) early T_{EFF} (6 *dpi*, 4 and 3 replicates, respectively), Runx3 binding sites in WT or *Runx3*$^{-/-}$ early T_{EFF} cells (4 *dpi*) and Tbet binding sites in WT or *Tbx21*$^{-/-}$ effector $CD8^+$ T cells (6 *dpi*) following an improved protocol[67] with minor modifications. In brief, the sort-purified cells (~1×10^5 cells for each replicate) were fixed with 1% formaldehyde for 10 min at room temperature and then suspended in RIPA buffer (10 mM Tris-HCl pH7.5, 1 mM EDTA, 150 mM NaCl, 0.2% SDS, 0.1% w/v sodium deoxycholate, and 1% Triton X-100) for nuclei extraction. The nuclei were then incubated with 0.5 μg rabbit anti-Tle3 polyclonal antibody (11372–1-AP, Proteintech), rabbit anti-Runx3 polyclonal antibody (Ab11905, Abcam), rabbit anti-Tbet polyclonal antibody (13700–1-AP, Proteintech), or rabbit IgG in antibody-binding buffer (10 mM Tris-HCl pH7.5, 1 mM EDTA, 150 mM NaCl, and 1% Triton X-100) overnight with rotation. The unbound antibody was removed by washing the nucleus pellet with the Antibody-Binding buffer, and the nuclei were incubated with protein A/G-micrococcal nuclease (MNase) fusion protein (produced with prokaryotic expression plasmid from Addgene, plasmid #123461) for one hour at 4°C. The unbound MNase was removed by washing with Wash buffer (10 mM Tris-HCl pH7.5, 1 mM EDTA, 400 mM NaCl, and 1% Triton X-100). After suspended in Resuspension buffer (20 mM Tris-HCl pH7.5, 10 mM NaCl, and 0.1% Triton X-100), the antibody-bound MNase was activated by

addition of $CaCl_2$ (final concentration 2 mM) followed by 30 min incubation at 0°C. The reaction was quenched with Stopping buffer (20 mM Tris,-HCl pH 8.0, 10 mM EGTA, 20 mM NaCl, 0.2% SDS, and 0.2 μg/μl proteinase K), and then incubated at 65°C for 2 hrs to reverse the crosslinking. The DNA fragments were purified with MinElute Reaction Cleanup kit (QIAGEN), end-repaired, adaptor added and then amplified with PCR for 10–14 cycles with barcoded Nextera primers (Illumina). The amplified DNA fragments in the range of 150–1,000 bp were recovered from 2% E-Gel EX Agarose Gels (Invitrogen/ThermoFisher Scientific). The libraries were quantified using a KAPA Library Quantification kit (Roche) and sequenced on Illumina HiSeq4000 in paired-end read mode with the read length of 150 nucleotides at the Admera Health. The Tle3 CUT&RUN data were deposited at the GEO (GSE213036 and GSE241534) under the SuperSeries of GSE213041.

Data processing.—The sequencing quality of the libraries was assessed by FastQC v0.11.9 (http://www.bioinformatics.babraham.ac.uk/projects/fastqc/). The Trimmomatic (v.0.39) was used to retain 36 bp from 5'-end of the sequence. Bowtie2 v2.4.4 [68] was used to align the sequencing reads to the mm10 mouse genome, and only uniquely mapped reads (MAPQ≥30) were retained. Samtools 1.13 [69] was used to transfer the sam files to bam files and sort bam files. Picard MarkDuplicates 2.26.0 (https://github.com/broadinstitute/picard) was used to remove duplicate reads in the bam files. MACS v2.2.7.1[37] was used for Tle3 peak calling (paired-end mode, FDR<0.05), and Tle3 binding peaks in each cell type were called by applying MACS2 to the reads pooled from biological replicates.

Reproducibility analysis.—The Tle3 binding peaks called by MACS2 from four cell types (a total of 9 biological replicates) were merged into 34,292 union peaks. Raw counts in each library were mapped onto those union peaks, resulting in a 34,292 × 9 matrices with rows representing the peaks and columns representing the libraries. The raw-count matrices were then subjected to normalization as follows: each row, representing a peak region, was normalized by length of each peak region per kilobase (also used as peak signal score) and each column, representing a library, was then normalized by the column sum per million. The normalized matrices were subjected to PCA analysis.

Identification of dynamic Tle3 binding clusters during $CD8^+$ T cell response.—Tle3 binding sites in T_N, T_{EFF}, T_{EM} and T_{CM} replicates were used to generate 34,292 × 9 raw-count matrices, which were used as input for DESeq2 (v.1.32.0)[70] to identify dynamic Tle3 binding peaks. To identify the most significant, high-confidence changes in Tle3 binding strength during $CD8^+$ T cell responses, stringent criteria were applied as the following: ≥3-fold binding strength changes, FDR<0.1, and the peak signal score (as defined above) ≥0.7 in cell type with higher binding strength. From 3 key comparison of T_{EFF}, T_{EM}, or T_{CM} with T_N cells, 3,627 dynamic Tle3 binding peaks were identified (as in Extended data Fig. 3c), and the corresponding 3,627 rows were extracted from the normalized 34,292 × 9 matrices and subjected to row-wise z-score transformation. The dynamic Tle3 peaks were separated into 3 major clusters based on K-means clustering analysis.

For specific analysis of less dynamic Tle3 binding peaks in memory $CD8^+$ T cells, Tle3 binding peaks in T_{CM} and T_{EM} cells were called, and those overlapping with the 34,292 union peaks (defined from four cell types as above) were retained. The resulting 23,089 Tle3

binding peaks contained 3,041 dynamic Tle3 peaks, and the remainder 20,048 peaks were defined as less dynamic Tle3 peaks for downstream analysis.

For comparative analysis of Tle3 binding strength between WT and *TRKO* early T_{EFF} and that between WT and *TbetKO* early T_{EFF} cells, Tle3 binding peaks were called using genomic background with llocal=7500 and by the criteria of ≥2 fold enrichment and FDR<0.05, and then peaks called in IgG CUT&RUN samples were excluded from downstream analyses.

Analyses of Tle3 binding sites.—The distribution of dynamic Tle3 binding sites was determined with ChIPseeker's *annotatePeak* function [71], where promoter region was defined as +/–1kb region flanking TSS. For motif analysis, HOMER (v4.10.0) [41] was used with default parameters, and the top motifs were extracted with the corresponding statistics (*p*-value and percentage of targets). For functional annotation, the Genomic Regions Enrichment of Annotations Tool (GREAT, v.4.0.4) was used with default settings [39].

ATAC-seq and data analysis.

WT or *Tle3*$^{-/-}$ T_{EM} and T_{CM} cells were sort-purified in 2–3 biological replicates for each cell type, and *ex vivo* cultured WT or *Tle3*$^{\Delta CreET}$ T_{EM} cells were re-sorted for viable cells and collected in 2–3 replicates. Approximately 1×10^4 cells were used for ATAC-seq library preparation as previously described[50]. In brief, the sorted cells were treated in lysis buffer for 3 min on ice, and the extracted nuclei were resuspended in transposition mix containing 0.5 μl Transposase (Illumina) and incubated at 37°C for 30 min. The products were purified with MinElute Reaction Cleanup Kit (Qiagen) and then amplified with PCR for 13 cycles using barcoded Nextera primers (Illumina). DNA fragments in the range of 150–1,000 bp were recovered from 2% E-Gel EX Agarose Gels (Invitrogen, ThermoFisher Scientific). The libraries were quantified using a KAPA Library Quantification kit and sequenced on Illumina HiSeq4000 in paired-end read mode with the read length of 150 nucleotides at the Admera Health. The ATAC-seq data were deposited in the GEO (accession number GSE213035 and GSE241533) under the SuperSeries of GSE213041.

Data processing.—The sequencing quality of the libraries was assessed by FastQC v0.11.9. The Trimmomatic (v.0.39) was used to retain 36 bp from 5'-end of the sequence. Bowtie2 v2.4.4 [68] was used to align the sequencing reads to the mm10 mouse genome, and only uniquely mapped reads (MAPQ≥30) were retained. Samtools 1.13 [69] was used to transfer the sam files to bam files and sort bam files. Picard MarkDuplicates 2.26.0 (https://github.com/broadinstitute/picard) was used to remove duplicate reads in the bam files. MACS v2.2.7.1 [37] was used for ATAC-seq peak calling (paired-end mode, FDR<0.05), and ATAC-seq peaks in each cell type were called by applying MACS2 to the reads pooled from biological replicates.

Reproducibility analysis.—The ATAC-seq peaks called by MACS2 from four cell type/states (*i.e.*, WT or *Tle3*$^{-/-}$ T_{EM} and T_{CM} cells, a total of 10 biological replicates) were merged into 55,158 union peaks, which were defined as union chromatin accessibility (ChrAcc) sites. Raw counts in each library were mapped onto those union ChrAcc

sites, resulting in a 55,158×10 matrices with rows representing the peaks and columns representing the libraries. The raw-count matrices were then subjected to normalization as follows: each row, representing a peak region, was normalized by length of each peak region per kilobase (also used as ChrAcc site signal score) and each column, representing a library, was then normalized by the column sum per million. The normalized matrices were subjected to PCA analysis.

Identification of differential ChrAcc clusters.—The 55,158×10 raw-count matrices were used as input for DESeq2 (v.1.32.0) [70] to identify differential ChrAcc sites between two cell types/states. To define T_{CM} and T_{EM} signature ChrAcc sites through WT T_{CM} *vs.* WT T_{EM} cell comparison, the criteria were applied as the following: ≥2-fold ChrAcc signal strength changes, FDR<0.05, and the ChrAcc site signal score (as defined above) ≥0.15 in cell type with higher ChrAcc signal strength (Fig. 3B). To identify the most significant, high-confidence changes in ChrAcc caused by Tle3 deficiency in memory $CD8^+$ T cells, more stringent criteria were used in comparisons between WT and *Tle3*$^{-/-}$ T_{EM}, and WT and *Tle3*$^{-/-}$ T_{CM} cells as the following: ≥3-fold ChrAcc signal strength changes, FDR<0.05, and the ChrAcc site signal score (as defined above) ≥0.15 in cell type with higher ChrAcc signal strength (Extended data Fig. 3e). From the WT and *Tle3*$^{-/-}$ cell comparisons, 5,553 differential ChrAcc sites were identified (as in Fig. 4C), and the corresponding 5,553 rows were extracted from the normalized 55,158×10 matrices and subjected to row-wise z-score transformation. The differential ChrAcc sites were separated into 8 distinct clusters based on K-means clustering analysis.

Association of Tle3 binding sites and/or Diff ChrAcc sites with DEGs.

For assignment of dynamic Tle3 peaks or Diff ChrAcc sites to their target genes, a site that appears within +/–100 kb flanking region of gene TSS was considered to be associated with that gene. Sites located within +/– 1 kb from the TSS were designated as promoter-associated sites, and other sites outside the promoter regions were designated as distal sites. Note that one Tle3 binding or ChrAcc site could be associated with more than one unique Refseq gene(s).

Statistical analysis.

For comparison between two experimental groups, Student's *t*-test was used. For multiple group comparisons, one way ANOVA was used to first determine whether any of the differences between the means are statistically significant, followed by 1) unpaired Student's *t*-test to determine the statistical significance for a specific pair, or 2) post hoc Tukey's multiple comparisons test to more stringently determine the statistical significance of differences between all possible pairs.

Extended Data

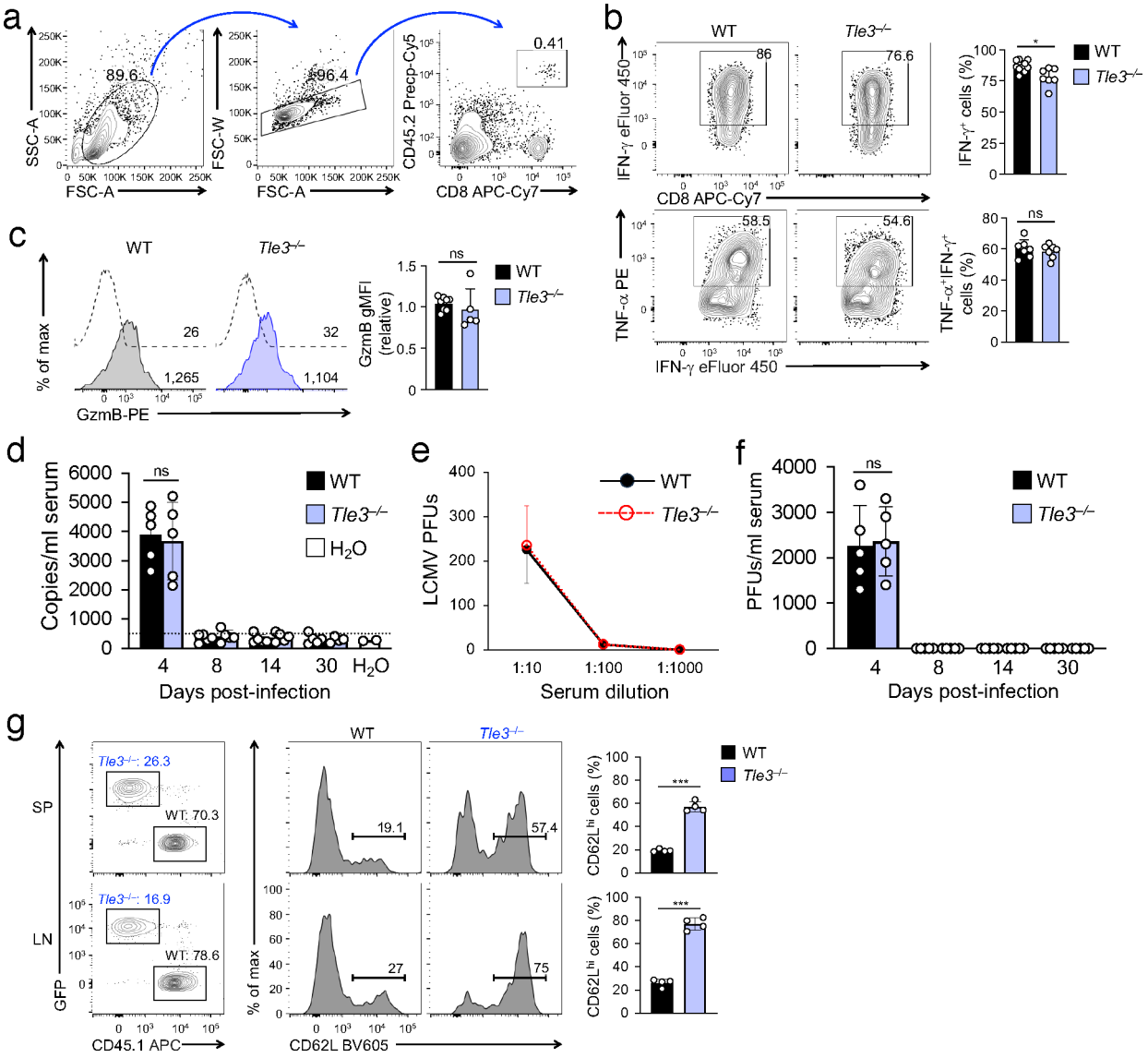

Extended Data Figure 1. Ablating Tle3 shows modest impact on the functions of antigen-responding CD8$^+$ T cells without affecting viral clearance.

a. Gating stratey to identify CD45.2$^+$ donor-derived P14 CD8$^+$ T cells in CD45.1$^+$ wild-type recipients.

b. Detection of cytokine production in effector CD8$^+$ T cells on 8 *dpi*. CD45.2$^+$ wild-type or *Tle3*$^{-/-}$ naive CD8$^+$ T cells were transferred into CD45.1$^+$ wild-type recipients, which were infected with LCMV-Arm the next day, following experimental design in Fig. 1c. GP33-induced production of IFN-γ (top) and TNF-α (bottom) was detected in CD45.2$^+$CD8$^+$ T cells. Representative contour plots (left) are from 2 independent experiments, with values denoting percentages of the gated population. Cumulative data (right) of the percentage of IFN-γ$^+$ population in P14 CD8$^+$ T cells and the percentage of TNF-α$^+$ populations in IFN-γ$^+$ P14 CD8$^+$ T cells are means ± s.d.

c. Detection of granzyme B expression in effector CD8$^+$ T cells by intracellular staining on 8 *dpi*. Representative histographs (left) are from 2 independent experiments, with the values denoting geometric mean fluorescence intensity (gMFI) of granzyme B. Cumulative data (left) are means ± s.d. ns, not statistically significant; *, p<0.05; ***, p<0.001 as determined with two-tailed Student's *t*-test.

d–f. Detection of LCMV in recipient sera. The serum samples were collected from recipients of WT or *Tle3*$^{-/-}$ CD8$^+$ T cells at the indicated time points, and LCMV was detected with either quantitative RT-PCR (**d**) or plaque assays (**e, f**). Note that in the plaque assay, sera were serially diluted for the measurement as exemplifed for the 4 *dpi* samples (**e**), and plaque forming units (PFUs) at 1:10 dilution were plotted for all time points (**f**).

g. Detection of T_{CM} frequency at ≥30 *dpi* in the spleen (SP) and lymph nodes (LN) of CD45.1$^+$ recipients where CD45.2$^+$ *Tle3*$^{-/-}$ and CD45.1$^+$ CD45.2$^+$ WT P14 cells were mixed for co-transfer, followed by LCMV-Arm infection. Donor-derived T_M cells were identified firstly by gating on CD45.2$^+$ cells, in which CD45.1$^+$ cells were from WT (black) while CD45.1$^-$GFP$^+$ cells were from *Tle3*$^{-/-}$ (blue).

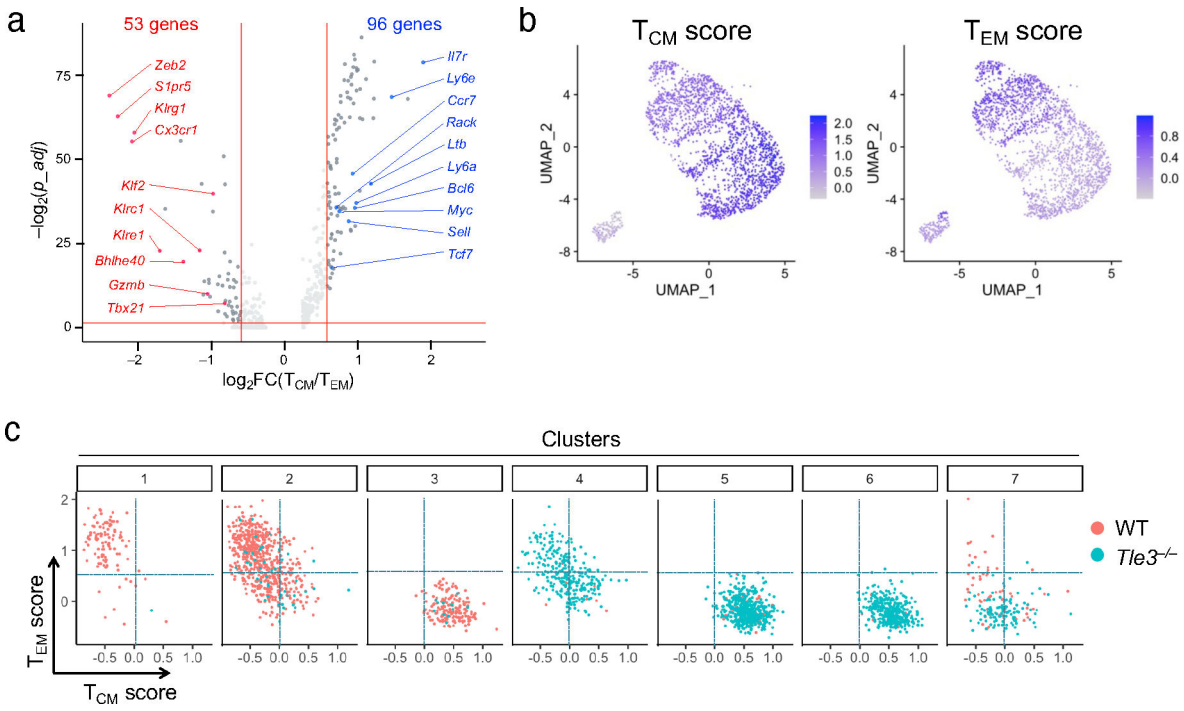

Extended Data Figure 2. Targeting Tle3 promotes expression of T_{CM} signature genes on the single cell level.

a. Volcano plot showing differential gene expression between the T_{CM} and T_{EM}1/2 clusters based on scRNA-seq analysis of WT memory CD8$^+$ T cells. 96 T_{CM} and 53 T_{EM} signature genes were identified by the criteria of ≥1.5 expression changes and FDR<0.05.

b. UMAP plots of WT and *Tle3*$^{-/-}$ cells displaying T_{CM} and T_{EM} scores for single cells. The scores for each cell were calcuated based on the expression of 96 T_{CM} and 53 T_{EM} signature genes defined in **a**, using Seurat's "*AddModuleScore*" function.

c. Scatter plots showing T_{CM} and T_{EM} scores for cells in each of the seven clusters as defined in Fig. 2e, with WT and *Tle3*$^{-/-}$ cells coded in distinct colors.

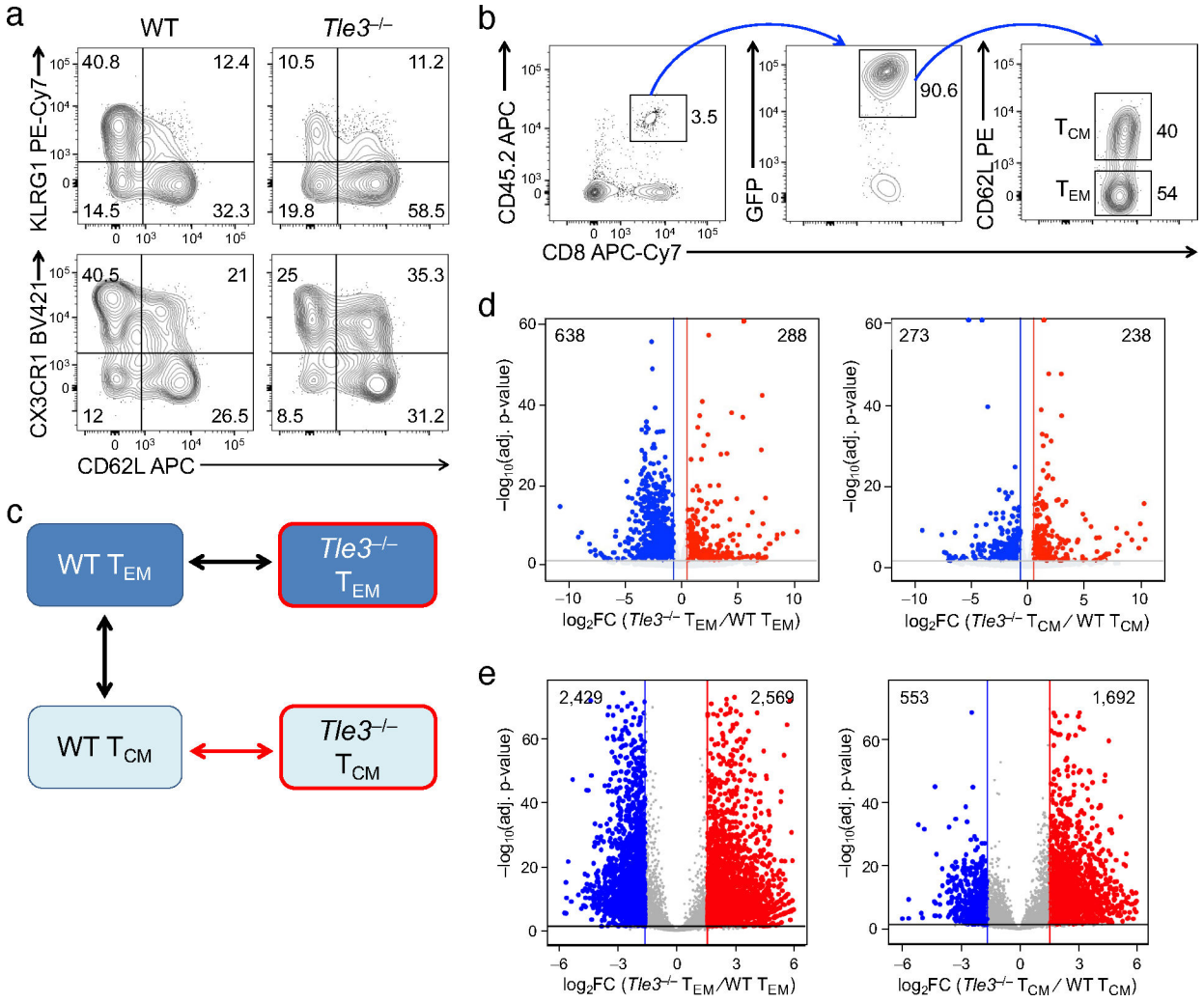

Extended Data Figure 3. Targeting Tle3 promotes T_{CM}- but diminishes T_{EM}-chracteristic molecular features.

a. Phenotypic analysis of WT and *Tle3*$^{-/-}$ P14 T_M cells at ≥30 *dpi* based on select cell surface markers.

b. Gating strategy for cell sorting of WT and *Tle3*$^{-/-}$ T_{CM} and T_{EM} cells.

c. Key comparisons for analysis of transcriptomic and ChrAcc changes in this study.

d. Volcano plots showing DEGs between WT and *Tle3*$^{-/-}$ T_{EM} cells (left) and those between WT and *Tle3*$^{-/-}$ T_{CM} cells (right) by the criteria of ≥1.5-fold expression changes, FDR<0.05, and FPKM≥0.5 in the higher expression condition. Values in the plot denote DEG numbers in each pairwise comparison.

e. Volcano plots showing differential ChrAcc sites between WT and *Tle3*$^{-/-}$ T_{EM} cells (left) and those between WT and *Tle3*$^{-/-}$ T_{CM} cells (right) by a more stringent criteria of ≥3-fold signal strength changes and FDR<0.05. Values in the plot denote numbers of differential ChrAcc sites in each pairwise comparison.

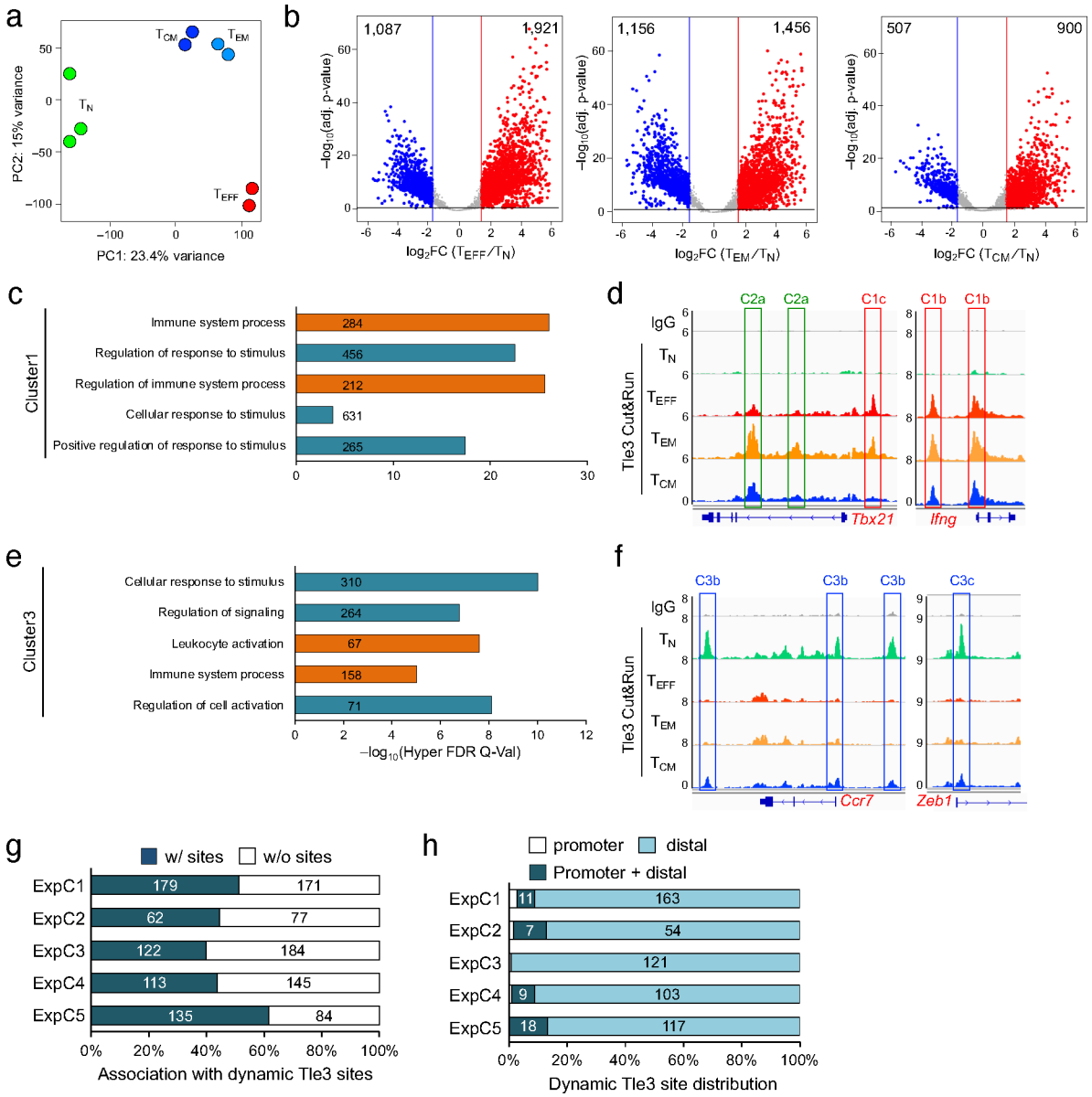

Extended Data Figure 4. Differential Tle3 binding is associated with immune regulation during CD8$^+$ T cell responses.

a. Principal component analysis (PCA) of Tle3 CUT&RUN libraries from WT T_N, T_{EFF}, T_{EM} and T_{CM} cells.

b. Volcano plots showing differential Tle3 binding sites in comparisons of T_{EFF}, T_{EM} and T_{CM} with T_N cells, where stringent criteria (≥3-fold difference in binding strength, adjusted *p* value <0.05) were used to define dynamic Tle3 binding sites. Values in plots denote numbers of dynamic Tle3 binding sites in each comparison.

c,e. Functional annotation of dynamic Tle3 binding sites in clusters 1 (**c**) and 3 (**e**) using GREAT analysis, with GO terms associated with immune regulation highlighted in orange. Values denote Hyper Observed Gene hits.

d,f. Tle3 CUT&RUN sequencing tracks showing cluster 1 (**d**) or 3 (**f**) Tle3 binding sites at select genes as displayed on IGV, with the dynamic Tle3 binding sites marked with open

bars and subcluster information labeled. IgG CUT&RUN in T_N cells was used as a negative control.

g. Detection frequency of dynamic Tle3 sites within +/–100 kb of TSS of DEGs in the five expression clusters defined in Fig. 3c. Values denote numbers of DEGs that are assocatied with dynamic Tle3 sites and those that are not (w/o).

h. Distribution of DEG-associated dynamic Tle3 binding sites in genomic regions. From panel **g**, the DEGs associated with dynamic Tle3 peaks are divided into three categories, based on Tle3 site locations in promoters, distal regulatory regions, or both; and the values denote DEG numbers in each category.

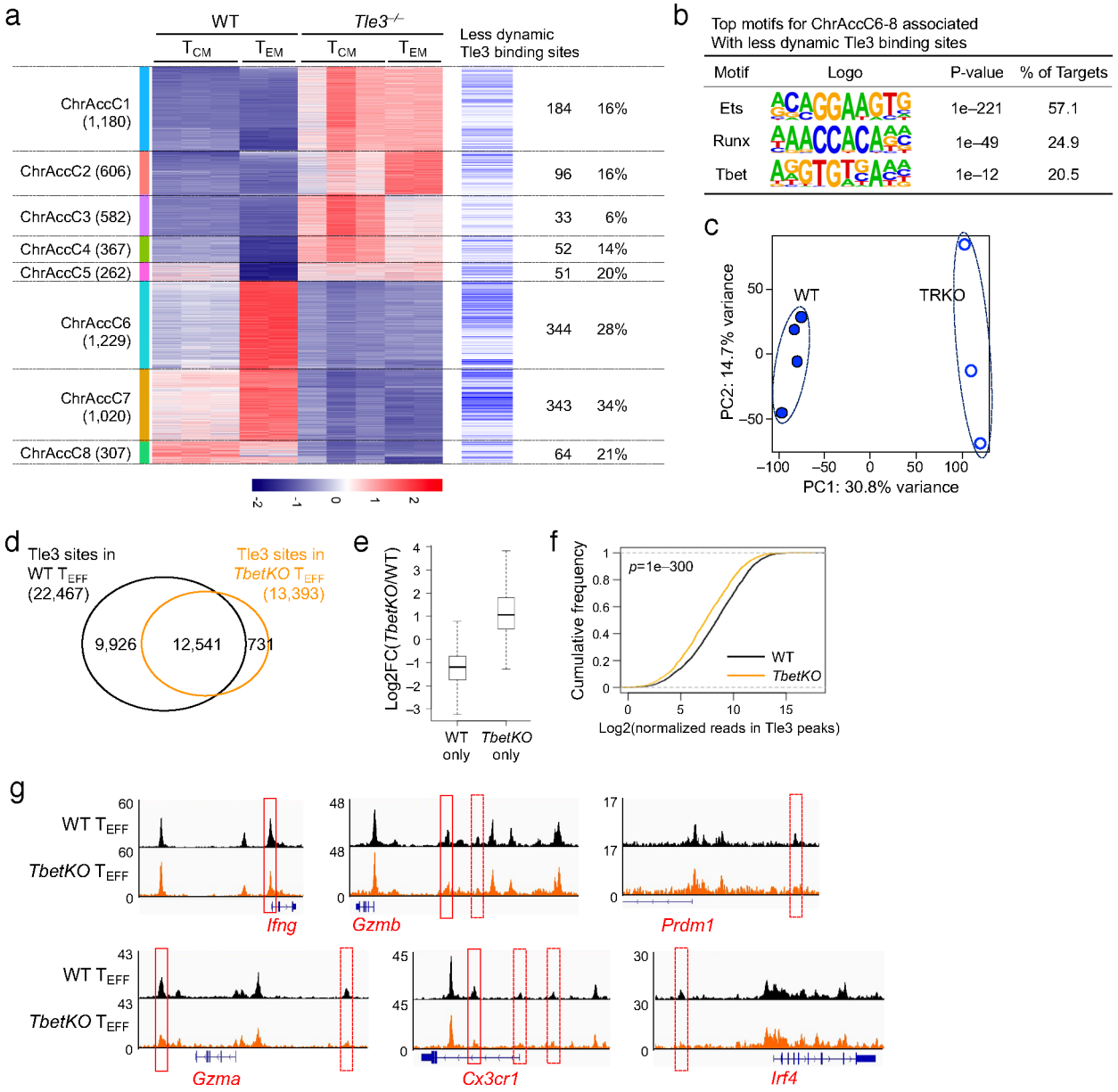

Extended Data Figure 5. Tle3 recruitment and stabilized binding require Runx3 and Tbet.

a. Stratification of less dynamic Tle3 binding sites with differential ChrAcc clusters as defined in Fig. 4c. Marked on the right are numbers and percentage of ChrAcc sites overlapping with less dynamic Tle3 binding peaks.

b. *De novo* motif analysis of ChrAcc clusters 6–8 (Fig. 4c, Tle3-opened) that overlapped with "less dynamic" Tle3 binding sites.

c. Principal component analysis (PCA) of Tle3 CUT&RUN sequencing libraries from WT and *TRKO* early T_{EFF} cells isolated on 4 *dpi*.

d. Venn diagram showing the overlap of Tle3 binding sites identified in WT and *TbetKO* T_{EFF} cells. Tle3 CUT&RUN was performed on WT (4 replicates) and *TbetKO* (in 3 replicates) T_{EFF} cells isolated on *6 dpi*. *Note that a single Tle3 binding site called in one cell type could overlap with more than one sites in the other, and therefore, the sum of common and uniquely identified Tle3 binding sites in the Venn diagram is not necessarily equal to the total site numbers called in a specific cell type.*

e. Boxplot showing the ratio of Tle3 binding strength in *TbetKO* to WT T_{EFF} cells for Tle3 binding sites uniquely detected in each cell type. The box center lines denote the median, box edge denotes interquartile range (IQR), and whiskers denote the most extreme data points that are no more than 1.5 × IQR from the edge.

f. Cumulative frequency plot showing differential Tle3 binding strength in WT *versus* *TbetKO* T_{EFF} cells at the 3,380 Tbet/Runx-dependent Tle3 binding sites (defined in Fig. 5f). Statitistical significance of the observed difference was determined with two-sided paired MWU test.

g. Sequencing tracks of Tle3 CUT&RUN in WT and *TbetKO* T_{EFF} cells. Rectangles with solid lines denote differential Tle3 binding sites with *TbetKO* cells showing ≥1.25-fold decrease in binding strength with FDR<0.05, while those with dotted lines denote Tle3 binding sites indentifed in WT but not *TbetKO* T_{EFF} cells by the same peak calling criteria.

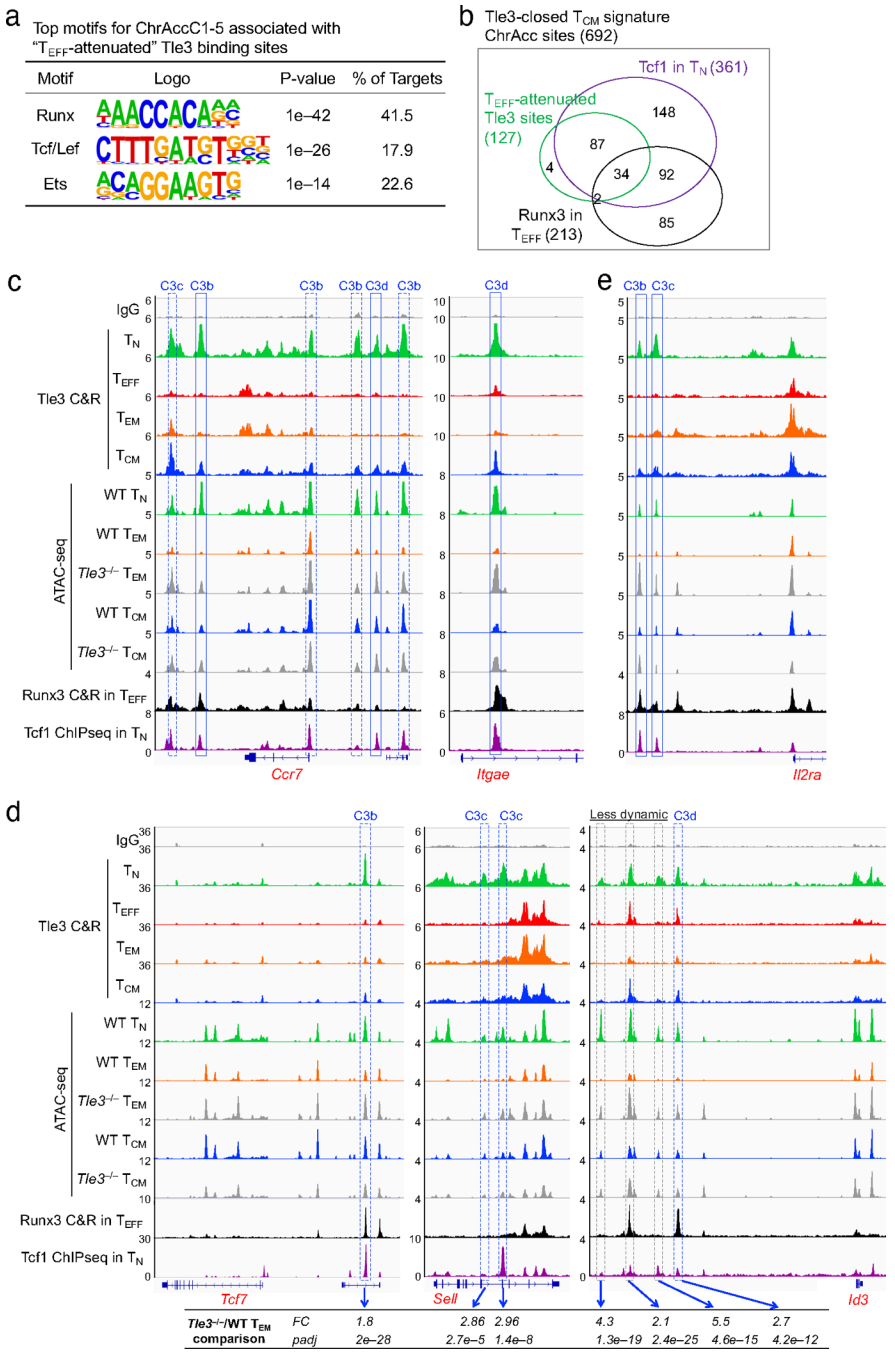

Extended Data Figure 6. Tle3 restrains chromatin opening at T_{CM} signature ChrAcc sites via direct and indirect means.

a. *De novo* motif analysis of ChrAcc clusters 1–5 that overlapped with "T_{EFF}-attenuated" Tle3 binding sites (within blue square in Fig. 4e).

b. Venn diagram showing overlap of "T_{EFF}-attenuated" Tle3 binding sites with Tcf1 binding sites in T_N and Runx3 binding sites in T_{EFF} cells at Tle3-closed T_{CM} signature ChrAcc sites (from ChrAccC1–5 with red bars in Fig. 4c).

c,d. Sequencing tracks of Tle3 binding (top), Tcf1 and Runx3 binding (bottom), and ChrAcc states (middle) at T_{CM}-characteristic genes as displayed on IGV. Open bars denote colocalized "T_{EFF}-attenuated" Tle3 binding peaks and Tle3-closed ChrAcc sites, with Tle3 binding subcluster information marked on the top. Bars with dotted lines at the *Ccr7* (**c**), *Tcf7, Sell* and *Id3* (**d**) gene loci mark dynamic Tle3 binding sites where the ChrAcc changes between WT and *Tle3*$^{-/-}$ T_{EM} cells did not reach the stringent ≥3-fold differences, while bars with grey dotted lines at the *Id3* gene locus (**d**) mark differential ChrAcc sites between WT and *Tle3*$^{-/-}$ T_{EM} cells, which are associated with "less dynamic" Tle3 binding sites (the Tle3 binding strength did not show ≥3fold changes during $CD8^+$ T cell responses). Statistical data in the comparison of the marked ChrAcc sites between WT and *Tle3*$^{-/-}$ T_{EM} cells are shown for *Tcf7, Sell* and *Id3* (**d**) genes under the tracks.

e. Tle3-bound, Tle3-closed ChrAcc sites can contribute to positive gene regulation, as observed at the *Il2ra* gene locus. *We posit that these Tle3-bound elements may have the potential to function as silencers, and the Tle3 binding likely maintains their inactive state, allowing their target genes to be expressed/induced in WT cells. Loss of Tle3 resulted in increased ChrAcc at these elements, unleashing the silencer activity and hence leading to target gene repression.*

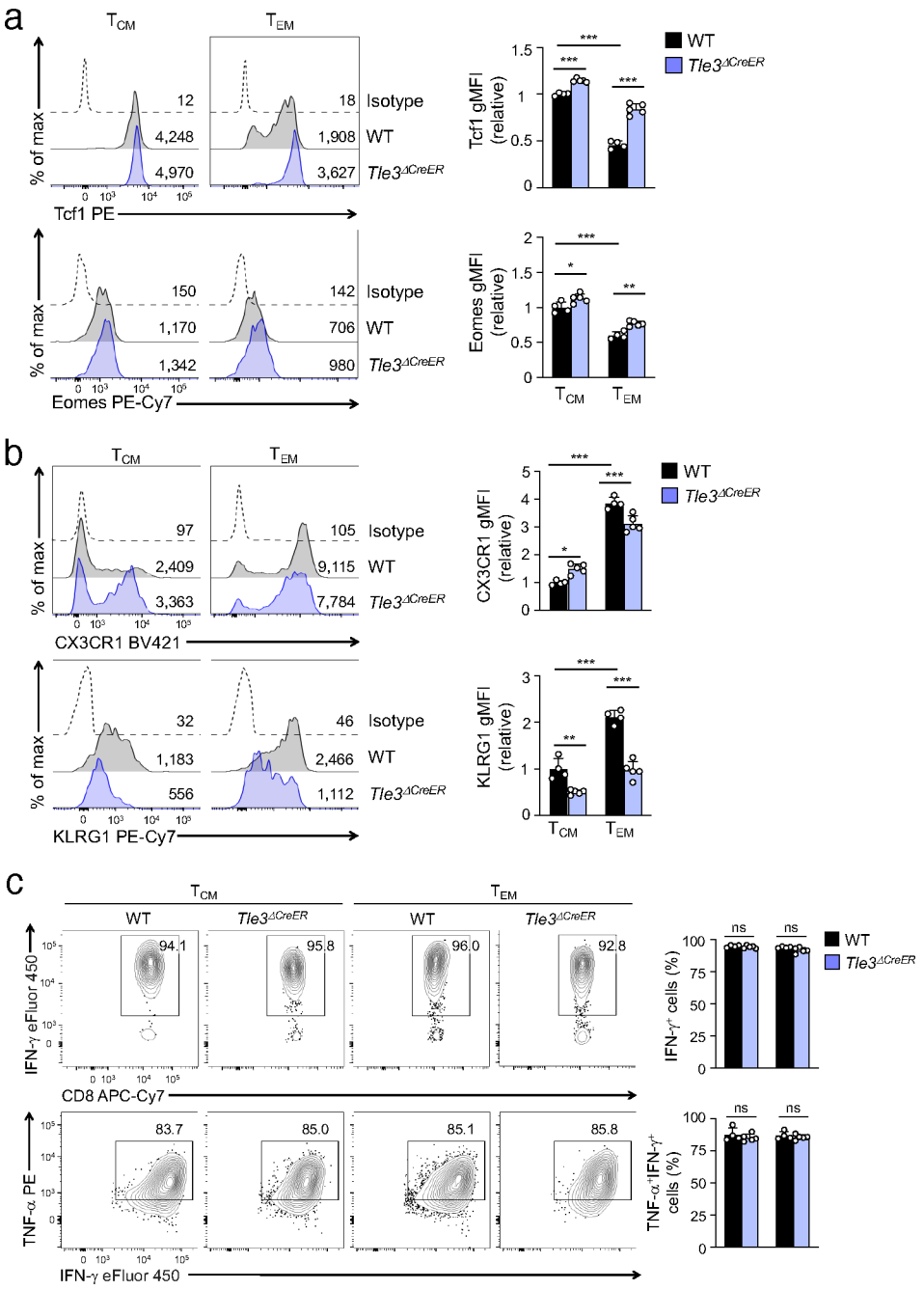

Extended Data Figure 7. Induced deletion of Tle3 at the effector phase promotes T_{CM} cell features without detectably affecting T_M cell functions.

a–b. Detection of T_{CM} (**a**) and T_{EM} (**b**) characteristic proteins with flow cytometry. CreER$^+$ *Tle3*$^{+/+}$ (WT) and CreER$^+$ *Tle3*$^{FL/FL}$ (*Tle3*$^{\Delta CreER}$) P14 cells were adoptively transferred, followed by LCMV-Arm infection. The recipients were treated with Tamoxifen on 6 and 7 *dpi* to achieve Tle3 deletion at the effector phase, and treated again on 21 *dpi* to sustain Tle3 deletion (as in Fig. 6d). At ≥35 *dpi*, donor-derived P14 memory CD8$^+$ T cells in the recipient spleens were analyzed for T_{CM} and T_{EM}-characteristic proteins. Half-stacked histograms are representative data from at least 2 independent experiments with values

denoting gMFI. Cumulative data for each protein are means ± s.d., with individual data points shown.

c. Detection of cytokine production in GP33-stimulated T_{CM} and T_{EM} cells. Representative contour plots (left) are from 2 independent experiments, with values denoting percentages of the gated population. Cumulative data (right) of the percentage of IFN-γ^+ population in P14 $CD8^+$ T cells and the percentage of TNF-α^+ populations in IFN-γ^+ P14 $CD8^+$ T cells are means ± s.d.

For all panels, statistical significance for multiple group comparisons was first determined with one-way ANOVA, and Tukey's test was used as post-hoc correction for indicated pair-wise comparison. *, $p<0.05$; **, $p<0.01$; ***, $p<0.001$; ns, not statistically significant.

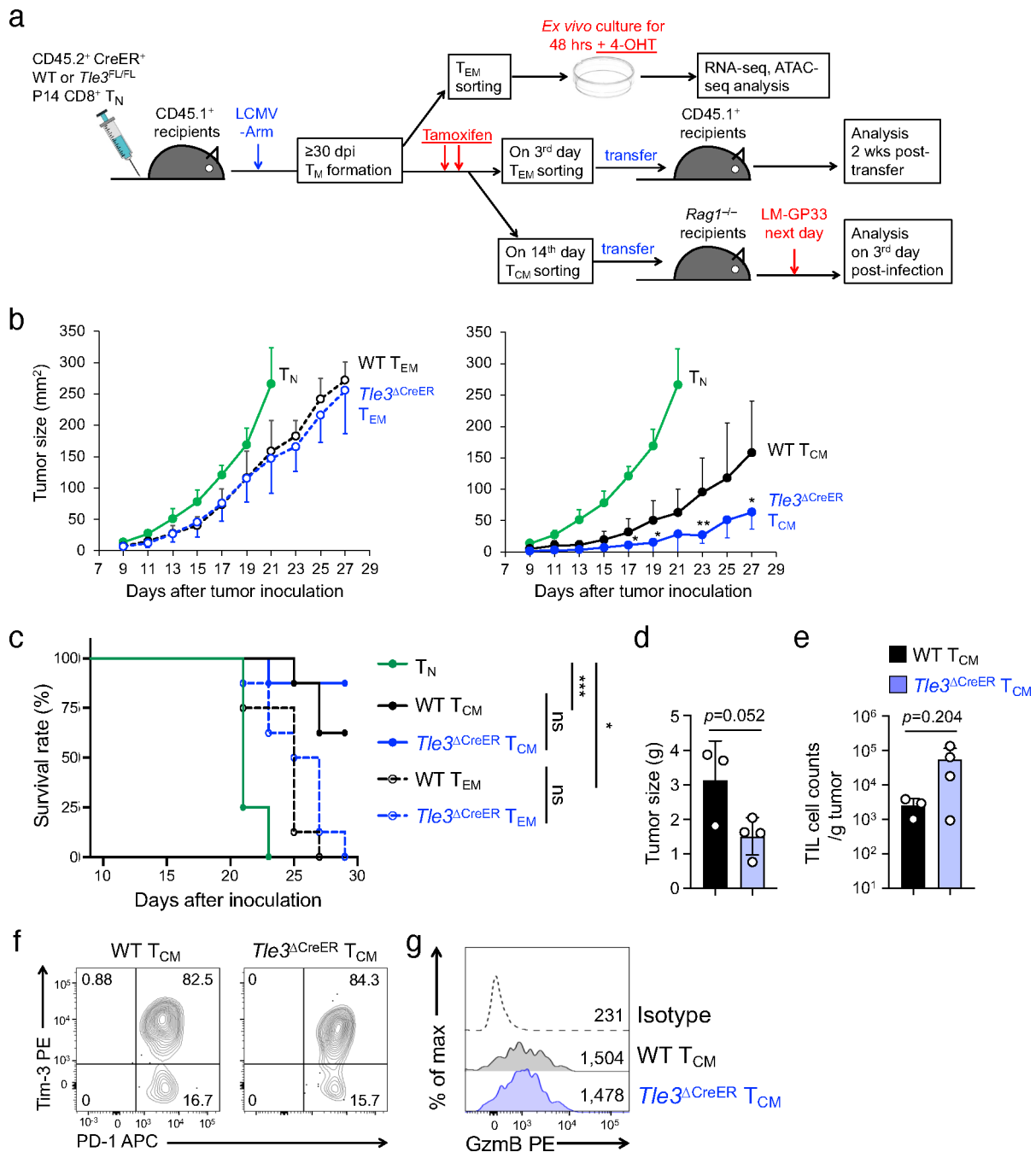

Extended Data Figure 8. Targetig Tle3 promotes T_{CM} cell formation without compromising its recall capacity.

a. Experimental design for investigating the impact of acute deletion of Tle3 in 'established' T_{EM} cells.

b–g. Assessment of T_{CM} recall response in B16 melanoma model. Note that WT and *Tle3*$^{\Delta CreER}$ T_{CM} cells were sort-purified following the study design in Fig. 6d. Data are from one of two independent experiments with similar results.

b. Kaplan-Meier survival curves of recipient mice that received 5´10^4 P14$^+$ T_N, WT or *Tle3*$^{\Delta CreER}$ T_{CM} or T_{EM} cells, followed by *s.c.* inoculation of B16-GP33 cells (2´10^5/mouse,

n=8 for each type of recipients). *, p<0.05; ***, p<0.001; ns, not statistically significant for indicated pair-wise comparison. Statistically insignificant time points are unmarked for clarity.

c. Tracking tumor growth in surviving recipient mice. *, p<0.05; **, p<0.01 for comparison between WT and *Tle3*^{DCreER} T_{CM} or T_{EM} cells.

d. Tumor size in recipients of WT or *Tle3*^{DCreER} T_{CM} cells that survived till day 33 after tumor inoculation,

e–g. Analyses of tumor-infiltrating $CD8^+$ lymphocytes (TILs) derived from WT or *Tle3*^{DCreER} T_{CM} cells in surviving recipients on day 33 after tumor inoculation, including cell counts (**e**), cell surface detection of Tim3 and PD-1 (**f**) and intracellular detection of granzyme B (**g**).

Supplementary Material

Refer to Web version on PubMed Central for supplementary material.

Acknowledgements

We thank the HMH-CDI Flow Cytometry Core facility (M. Poulus and W. Tsao) for cell sorting. We thank Drs Jianmin Wang (Roswell Park Comprehensive Cancer Center), Qing-Sheng Mi and Indra Adrianto (Henry Ford Health) for their input in possessing NextGen sequencing data. This study is supported in-part by grants from the NIH (AI121080, AI139874, and AI112579 to H.-H.X.) and the Veteran Affairs (BX005771 to H.-H.X.). Q.S. is supported by the CAMS Innovation Fund for Medical Sciences (2022-I2M-1–024, 2022-I2M-2–004, 2021-I2M-1–047), the Non-profit Central Research Institute Fund of Chinese Academy of Medical Sciences (2022-RC310–11). The authors declare no conflict of interests.

Data Availability

The Tle3 CUT&RUN, bulk RNA-seq, single-cell RNA-seq, and ATAC-seq data in $CD8^+$ T cells are deposited at the Gene Expression Omnibus under accession number GSE213041.

References

1. Akondy RS et al. Origin and differentiation of human memory CD8 T cells after vaccination. Nature 552, 362–367 (2017). [PubMed: 29236685]
2. Jameson SC & Masopust D Understanding Subset Diversity in T Cell Memory. Immunity 48, 214–226 (2018). [PubMed: 29466754]
3. Martin MD & Badovinac VP Defining Memory CD8 T Cell. Front Immunol 9, 2692 (2018). [PubMed: 30515169]
4. Sallusto F, Lenig D, Forster R, Lipp M & Lanzavecchia A Two subsets of memory T lymphocytes with distinct homing potentials and effector functions. Nature 401, 708–712 (1999). [PubMed: 10537110]
5. Wherry EJ et al. Lineage relationship and protective immunity of memory CD8 T cell subsets. Nature immunology 4, 225–234 (2003). [PubMed: 12563257]
6. Kaech SM et al. Selective expression of the interleukin 7 receptor identifies effector CD8 T cells that give rise to long-lived memory cells. Nature immunology 4, 1191–1198 (2003). [PubMed: 14625547]
7. Joshi NS et al. Inflammation directs memory precursor and short-lived effector CD8(+) T cell fates via the graded expression of T-bet transcription factor. Immunity 27, 281–295 (2007). [PubMed: 17723218]
8. Lin WW et al. CD8(+) T Lymphocyte Self-Renewal during Effector Cell Determination. Cell Rep 17, 1773–1782 (2016). [PubMed: 27829149]

9. Pais Ferreira D et al. Central memory CD8(+) T cells derive from stem-like Tcf7(hi) effector cells in the absence of cytotoxic differentiation. Immunity 53, 985–1000 e1011 (2020). [PubMed: 33128876]
10. Johnnidis JB et al. Inhibitory signaling sustains a distinct early memory CD8(+) T cell precursor that is resistant to DNA damage. Sci Immunol 6 (2021).
11. Chung HK, McDonald B & Kaech SM The architectural design of CD8+ T cell responses in acute and chronic infection: Parallel structures with divergent fates. J Exp Med 218 (2021).
12. Chen Y, Zander R, Khatun A, Schauder DM & Cui W Transcriptional and Epigenetic Regulation of Effector and Memory CD8 T Cell Differentiation. Front Immunol 9, 2826 (2018). [PubMed: 30581433]
13. Kallies A, Xin A, Belz GT & Nutt SL Blimp-1 transcription factor is required for the differentiation of effector CD8(+) T cells and memory responses. Immunity 31, 283–295 (2009). [PubMed: 19664942]
14. Gautam S et al. The transcription factor c-Myb regulates CD8(+) T cell stemness and antitumor immunity. Nature immunology 20, 337–349 (2019). [PubMed: 30778251]
15. Zhou X et al. Differentiation and persistence of memory CD8(+) T cells depend on T cell factor 1. Immunity 33, 229–240 (2010). [PubMed: 20727791]
16. Pipkin ME Runx proteins and transcriptional mechanisms that govern memory CD8 T cell development. Immunol Rev 300, 100–124 (2021). [PubMed: 33682165]
17. Shan Q et al. The transcription factor Runx3 guards cytotoxic CD8(+) effector T cells against deviation towards follicular helper T cell lineage. Nature immunology 18, 931–939 (2017). [PubMed: 28604718]
18. Orian A et al. A Myc-Groucho complex integrates EGF and Notch signaling to regulate neural development. Proceedings of the National Academy of Sciences of the United States of America 104, 15771–15776 (2007). [PubMed: 17898168]
19. Ren B, Chee KJ, Kim TH & Maniatis T PRDI-BF1/Blimp-1 repression is mediated by corepressors of the Groucho family of proteins. Genes & development 13, 125–137 (1999). [PubMed: 9887105]
20. Zhao X, Shan Q & Xue HH TCF1 in T cell immunity: a broadened frontier. Nat Rev Immunol 22, 147–157 (2022). [PubMed: 34127847]
21. Seo W & Taniuchi I The Roles of RUNX Family Proteins in Development of Immune Cells. Mol Cells 43, 107–113 (2020). [PubMed: 31926543]
22. Turki-Judeh W & Courey AJ Groucho: a corepressor with instructive roles in development. Curr Top Dev Biol 98, 65–96 (2012). [PubMed: 22305159]
23. Buscarlet M & Stifani S The 'Marx' of Groucho on development and disease. Trends in cell biology 17, 353–361 (2007). [PubMed: 17643306]
24. Jennings BH & Ish-Horowicz D The Groucho/TLE/Grg family of transcriptional co-repressors. Genome Biol 9, 205 (2008). [PubMed: 18254933]
25. Gasperowicz M & Otto F Mammalian Groucho homologs: redundancy or specificity? Journal of cellular biochemistry 95, 670–687 (2005). [PubMed: 15861397]
26. Xing S et al. Tle corepressors are differentially partitioned to instruct CD8(+) T cell lineage choice and identity. J Exp Med 215, 2211–2226 (2018). [PubMed: 30045946]
27. Wheat JC et al. The corepressor Tle4 is a novel regulator of murine hematopoiesis and bone development. PloS one 9, e105557 (2014). [PubMed: 25153823]
28. Ramasamy S et al. Tle1 tumor suppressor negatively regulates inflammation in vivo and modulates NF-kappaB inflammatory pathway. Proceedings of the National Academy of Sciences of the United States of America 113, 1871–1876 (2016). [PubMed: 26831087]
29. Rutishauser RL et al. Transcriptional repressor Blimp-1 promotes CD8(+) T cell terminal differentiation and represses the acquisition of central memory T cell properties. Immunity 31, 296–308 (2009). [PubMed: 19664941]
30. Zhao X et al. beta-catenin and gamma-catenin are dispensable for T lymphocytes and AML leukemic stem cells. Elife 9 (2020).

31. Wang D et al. The Transcription Factor Runx3 Establishes Chromatin Accessibility of cis-Regulatory Landscapes that Drive Memory Cytotoxic T Lymphocyte Formation. Immunity 48, 659–674 e656 (2018). [PubMed: 29669249]
32. Mahajan VS et al. DOCK2 Sets the Threshold for Entry into the Virtual Memory CD8(+) T Cell Compartment by Negatively Regulating Tonic TCR Triggering. J Immunol 204, 49–57 (2020). [PubMed: 31740487]
33. Cao J et al. The single-cell transcriptional landscape of mammalian organogenesis. Nature 566, 496–502 (2019). [PubMed: 30787437]
34. Herndler-Brandstetter D et al. KLRG1(+) Effector CD8(+) T Cells Lose KLRG1, Differentiate into All Memory T Cell Lineages, and Convey Enhanced Protective Immunity. Immunity 48, 716–729 e718 (2018). [PubMed: 29625895]
35. Gerlach C et al. The Chemokine Receptor CX3CR1 Defines Three Antigen-Experienced CD8 T Cell Subsets with Distinct Roles in Immune Surveillance and Homeostasis. Immunity 45, 1270–1284 (2016). [PubMed: 27939671]
36. Skene PJ & Henikoff S An efficient targeted nuclease strategy for high-resolution mapping of DNA binding sites. Elife 6 (2017).
37. Zhang Y et al. Model-based analysis of ChIP-Seq (MACS). Genome Biol 9, R137 (2008). [PubMed: 18798982]
38. Love MI, Huber W & Anders S Moderated estimation of fold change and dispersion for RNA-seq data with DESeq2. Genome Biol 15, 550 (2014). [PubMed: 25516281]
39. McLean CY et al. GREAT improves functional interpretation of cis-regulatory regions. Nat Biotechnol 28, 495–501 (2010). [PubMed: 20436461]
40. Guan T et al. ZEB1, ZEB2, and the miR-200 family form a counterregulatory network to regulate CD8(+) T cell fates. J Exp Med 215, 1153–1168 (2018). [PubMed: 29449309]
41. Heinz S et al. Simple combinations of lineage-determining transcription factors prime cis-regulatory elements required for macrophage and B cell identities. Molecular cell 38, 576–589 (2010). [PubMed: 20513432]
42. Levanon D et al. Transcriptional repression by AML1 and LEF-1 is mediated by the TLE/Groucho corepressors. Proceedings of the National Academy of Sciences of the United States of America 95, 11590–11595 (1998). [PubMed: 9751710]
43. Chen G & Courey AJ Groucho/TLE family proteins and transcriptional repression. Gene 249, 1–16 (2000). [PubMed: 10831834]
44. Liu J et al. CTCF mediates CD8+ effector differentiation through dynamic redistribution and genomic reorganization. J Exp Med 220 (2023).
45. Shan Q et al. Tcf1 and Lef1 provide constant supervision to mature CD8(+) T cell identity and function by organizing genomic architecture. Nat Commun 12, 5863 (2021). [PubMed: 34615872]
46. Shan Q et al. Tcf1-CTCF cooperativity shapes genomic architecture to promote CD8(+) T cell homeostasis. Nature immunology 23, 1222–1235 (2022). [PubMed: 35882936]
47. Zhao DM et al. Constitutive activation of Wnt signaling favors generation of memory CD8 T cells. J Immunol 184, 1191–1199 (2010). [PubMed: 20026746]
48. Shan Q et al. Tcf1 preprograms the mobilization of glycolysis in central memory CD8(+) T cells during recall responses. Nature immunology 23, 386–398 (2022). [PubMed: 35190717]
49. Milner JJ et al. Runx3 programs CD8(+) T cell residency in non-lymphoid tissues and tumours. Nature 552, 253–257 (2017). [PubMed: 29211713]
50. Shan Q et al. Ectopic Tcf1 expression instills a stem-like program in exhausted CD8(+) T cells to enhance viral and tumor immunity. Cell Mol Immunol 18, 1262–1277 (2021). [PubMed: 32341523]
51. Busch DH, Frassle SP, Sommermeyer D, Buchholz VR & Riddell SR Role of memory T cell subsets for adoptive immunotherapy. Semin Immunol 28, 28–34 (2016). [PubMed: 26976826]
52. Klebanoff CA et al. Central memory self/tumor-reactive CD8+ T cells confer superior antitumor immunity compared with effector memory T cells. Proceedings of the National Academy of Sciences of the United States of America 102, 9571–9576 (2005). [PubMed: 15980149]

53. Henning AN, Roychoudhuri R & Restifo NP Epigenetic control of CD8(+) T cell differentiation. Nat Rev Immunol 18, 340–356 (2018). [PubMed: 29379213]
54. Sharrocks AD The ETS-domain transcription factor family. Nat Rev Mol Cell Biol 2, 827–837 (2001). [PubMed: 11715049]
55. Anderson MK, Hernandez-Hoyos G, Diamond RA & Rothenberg EV Precise developmental regulation of Ets family transcription factors during specification and commitment to the T cell lineage. Development 126, 3131–3148 (1999). [PubMed: 10375504]
56. Villanueva CJ et al. TLE3 is a dual-function transcriptional coregulator of adipogenesis. Cell Metab 13, 413–427 (2011). [PubMed: 21459326]
57. Pearson S et al. Loss of TLE3 promotes the mitochondrial program in beige adipocytes and improves glucose metabolism. Genes & development 33, 747–762 (2019). [PubMed: 31123067]
58. Jacob J & Baltimore D Modelling T-cell memory by genetic marking of memory T cells in vivo. Nature 399, 593–597 (1999). [PubMed: 10376601]
59. Guo K et al. Disruption of peripheral leptin signaling in mice results in hyperleptinemia without associated metabolic abnormalities. Endocrinology 148, 3987–3997 (2007). [PubMed: 17495001]
60. McCausland MM & Crotty S Quantitative PCR technique for detecting lymphocytic choriomeningitis virus in vivo. J Virol Methods 147, 167–176 (2008). [PubMed: 17920702]
61. Sena-Esteves M, Tebbets JC, Steffens S, Crombleholme T & Flake AW Optimized large-scale production of high titer lentivirus vector pseudotypes. J Virol Methods 122, 131–139 (2004). [PubMed: 15542136]
62. Welsh RM & Seedhom MO Lymphocytic choriomeningitis virus (LCMV): propagation, quantitation, and storage. Curr Protoc Microbiol Chapter 15, Unit 15A 11 (2008).
63. Macosko EZ et al. Highly Parallel Genome-wide Expression Profiling of Individual Cells Using Nanoliter Droplets. Cell 161, 1202–1214 (2015). [PubMed: 26000488]
64. Dobin A et al. STAR: ultrafast universal RNA-seq aligner. Bioinformatics 29, 15–21 (2013). [PubMed: 23104886]
65. Hao Y et al. Integrated analysis of multimodal single-cell data. Cell 184, 3573–3587 e3529 (2021). [PubMed: 34062119]
66. Simon M, Grandage VL, Linch DC & Khwaja A Constitutive activation of the Wnt/beta-catenin signalling pathway in acute myeloid leukaemia. Oncogene 24, 2410–2420 (2005). [PubMed: 15735743]
67. Meers MP, Bryson TD, Henikoff JG & Henikoff S Improved CUT&RUN chromatin profiling tools. Elife 8 (2019).
68. Langmead B & Salzberg SL Fast gapped-read alignment with Bowtie 2. Nat Methods 9, 357–359 (2012). [PubMed: 22388286]
69. Li H et al. The Sequence Alignment/Map format and SAMtools. Bioinformatics 25, 2078–2079 (2009). [PubMed: 19505943]
70. Robinson MD, McCarthy DJ & Smyth GK edgeR: a Bioconductor package for differential expression analysis of digital gene expression data. Bioinformatics 26, 139–140 (2010). [PubMed: 19910308]
71. Yu G, Wang LG & He QY ChIPseeker: an R/Bioconductor package for ChIP peak annotation, comparison and visualization. Bioinformatics 31, 2382–2383 (2015). [PubMed: 25765347]

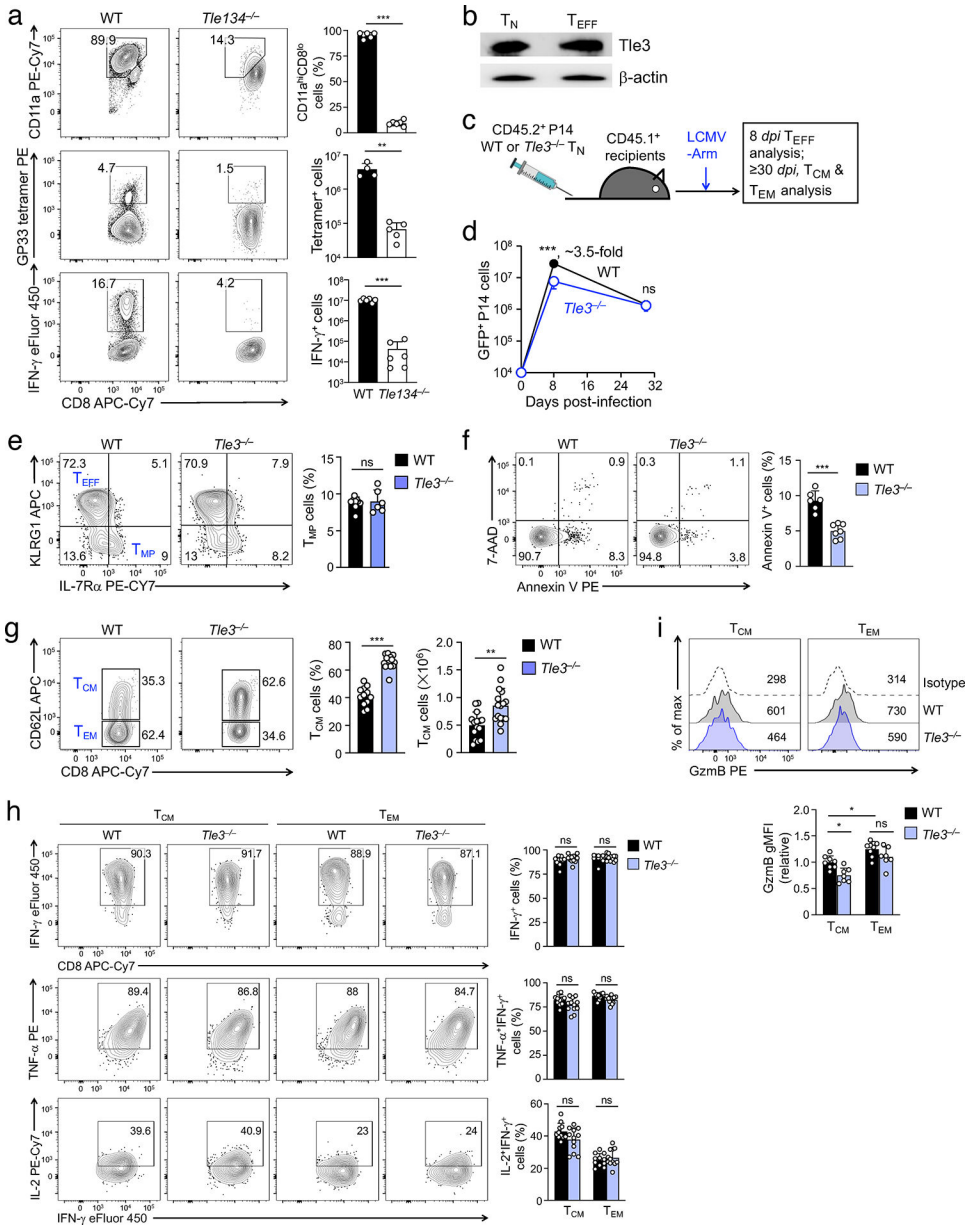

Figure 1. Targeting Tle3 favors generation of T_{CM} cells.

a. Detection of antigen-specific $CD8^+$ T cells in WT and *Tle134*$^{-/-}$ mice on 8 *dpi* with LCMV-Arm, using surrogate markers (top), GP33-tetramer (middle) and GP33 peptide-stimulated IFN-γ production (bottom). Shown in bar graphs are cumulative data on frequency of antigen-experienced $CD8^+$ T cells or numbers of GP33-specific $CD8^+$ T cells (right).

b. Detection of Tle3 in T_N and T_{EFF} (8 *dpi*) with immunoblotting. Data are representative from two independent experiments.

c. Experimental design. Naive P14 $CD8^+$ T cells were adoptive transferred into CD45-disparate recipients at 2×10^4 cells/recipient, followed by *i.p.* infection with LCMV-Arm and characterization of $CD8^+$ T cells at the effector and memory stages.

d. Numbers of WT and *Tle3*$^{-/-}$ P14 CD8^{+} T cells in recipient spleens at the effector (8 *dpi*) and memory (≥30 *dpi*) stages.

e. Detection of WT and *Tle3*$^{-/-}$ T_{EFF} and T_{MP} subsets on 8 *dpi*, with cumulative data on T_{MP} frequency in bar graph (right).

f. Detecting cell viability of antigen-specific CD8^{+} T cells during the contraction phase on 14 *dpi*, with cumulative data on frequency of AnnexinV^{+} cells in bar graphs (right).

g. Detection of WT and *Tle3*$^{-/-}$ T_{CM} and T_{EM} subsets at ≥30 *dpi*, with cumulative data on T_{CM} frequency and numbers in bar graphs (right).

h. Detection of GP33-induced cytokine production in T_{CM} and T_{EM} cells at ≥30 *dpi*. Cumulative data on the right show the frequency of IFN-γ-producing cells in CD45.2^{+} T_{CM} and T_{EM} cells (top), and that of TNF-α- and IL-2-producing cells in IFN-γ^{+} T_{CM} and T_{EM} cells (middle and bottom).

i. Detection of granzyme B expression in T_{CM} and T_{EM} cells at ≥30 *dpi*. In each experiment, the average of geometric mean fluorescence intensity (gMFI) of granzyme B in WT T_{CM} cells was set as 1, and the gMFI granzyme B in all cell types was normalized accordingly to obtain its relative expression, with cumulative data shown in bar graphs (bottom). Contour plots in **a**, **e–h** and half-stacked histograms in **i** are representative from 2–3 independent experiments, and all cumulative data are means ± s.d., with individual data points shown. *, $p<0.05$; **, $p<0.01$; ***, $p<0.001$; ns, not statistically significant by Student's *t*-test.

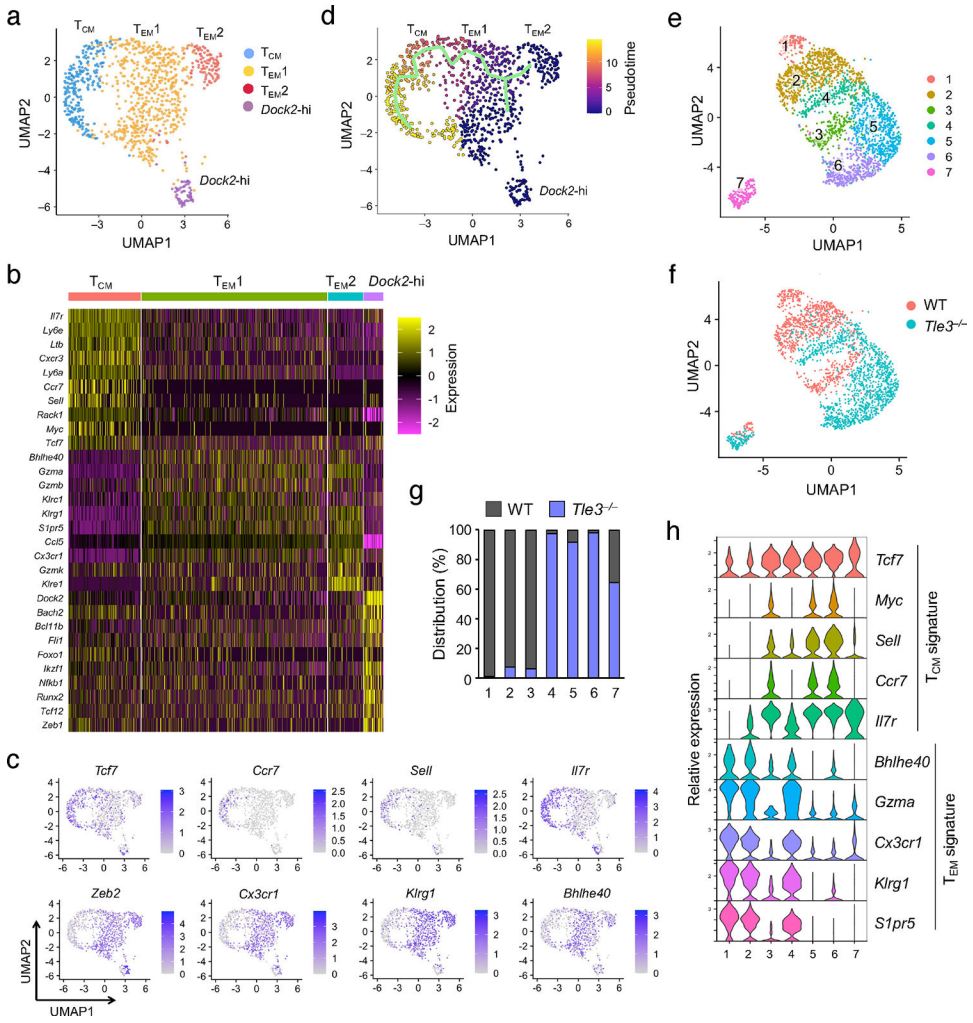

Figure 2. Targeting Tle3 promote T_{CM} formation on the single cell level.

a. UMAP plot of scRNA-seq data from WT memory P14 $CD8^+$ T cells sorted on 30 *dpi*, with each dot representing a single cell. A total of four clusters were identified with Seurat and color-coded.

b. Heatmap showing expression of 10 selected characteristic genes in T_{CM}, $T_{EM}1/2$ and *Dock2*-hi clusters as defined in **a**, with each column corresponding to a single cell. Color scale represents z-score transformed transcript levels.

c. Single-cell transcript levels of T_{CM} (top) and T_{EM} (bottom) signature genes as displayed in the UMAP plot. The range of transcript levels is marked with individual color scale for each gene.

d. Pseudotime analysis of WT memory P14 $CD8^+$ T cells using Monocle v3, with the green line showing the trajectory of convergency of $T_{EM}1/2$ to T_{CM} cells.

e–f. UMAP plots of scRNA-seq data from WT and *Tle3*$^{-/-}$ memory P14 $CD8^+$ T cells (30 *dpi*). Displayed in **e** are seven clusters identified with Seurat, and displayed in **f** are cells of different genotypes.

g. Distribution of WT and *Tle3*$^{-/-}$ cells in each cluster defined in **e**.

h. Violin plots showing transcript levels of T_{CM} and T_{EM} signature genes in each cluster defined in **e**.

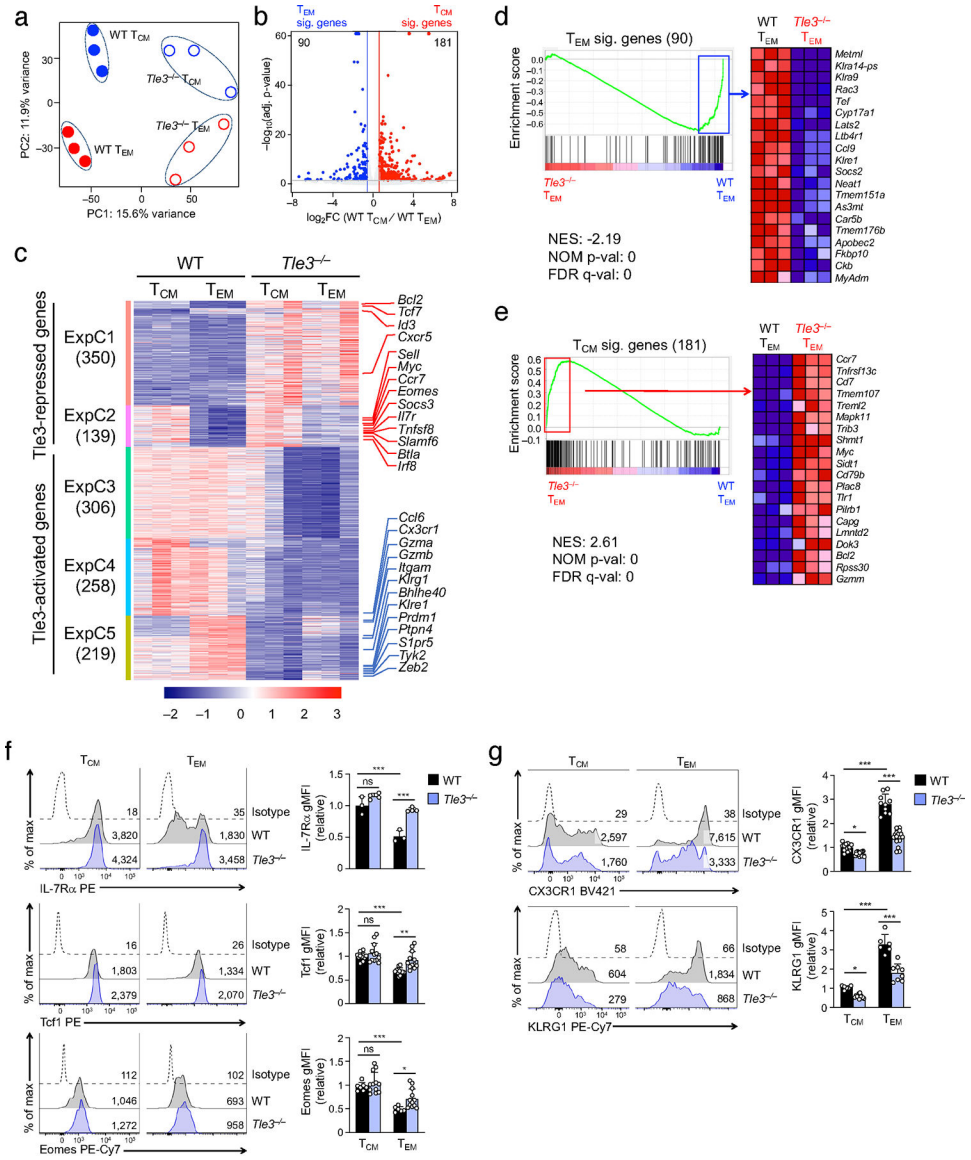

Figure 3. Targeting Tle3 promotes T_{CM} but diminishes T_{EM} signature gene expression.

a. Principal component analysis (PCA) of RNA-seq libraries from WT and *Tle3*$^{-/-}$ T_{CM} and T_{EM} cells (≥30 *dpi*).

b. Volcano plot showing DEGs between WT T_{CM} and WT T_{EM} cells based on bulk RNA-seq data by the criteria of ≥1.5-fold expression changes, FDR<0.05, and FPKM≥0.5 in the higher expression condition. Values in the plot denote numbers of T_{CM} and T_{EM} signature genes.

c. Heatmap showing the impact of Tle3 deficiency on T_{CM} and T_{EM} transcriptomes. DEGs were identified in comparison between WT and *Tle3*$^{-/-}$ T_{CM} and between WT and *Tle3*$^{-/-}$ T_{EM} cells, and were distributed into 5 major expression clusters (ExpC) with K-means clustering analysis. Values in parentheses denote gene numbers in each cluster, and select T_{CM} and T_{EM} signature genes are marked, as indicated with red and blue lines, respectively.

d–e. Enrichment plots of T_{EM} (**d**) and T_{CM} (**e**) signature gene sets (defined in **b**) in comparison of *Tle3*$^{-/-}$ vs. WT T_{EM} cell transcriptomes with GSEA. NES, normalized enrichment score; NOM *P* val, nominal *P* values. In **d**, 48 of 90 T_{EM} signature genes are in the leading edge showing enrichment in WT T_{EM} cells. In **e**, 104 of 181 T_{CM} signature genes are in the leading edge showing enrichment in *Tle3*$^{-/-}$ T_{EM} cells.

f–g. Detection of T_{CM} (**f**) and T_{EM} (**g**) characteristic proteins with flow cytometry in WT and *Tle3*$^{-/-}$ T_{CM} and T_{EM} cells at ≥30 *dpi*. Half-stacked histograms are representative data from at least 2 independent experiments with values denoting geometric mean fluorescence intensity (gMFI), and cumulative data for each protein are means ± s.d., with individual data points shown. Statistical significance for these multiple group comparisons was first determined with one-way ANOVA, and Tukey's test was used as post-hoc correction for indicated pair-wise comparison. *, $p<0.05$; **, $p<0.01$; ***, $p<0.001$; ns, not statistically significant.

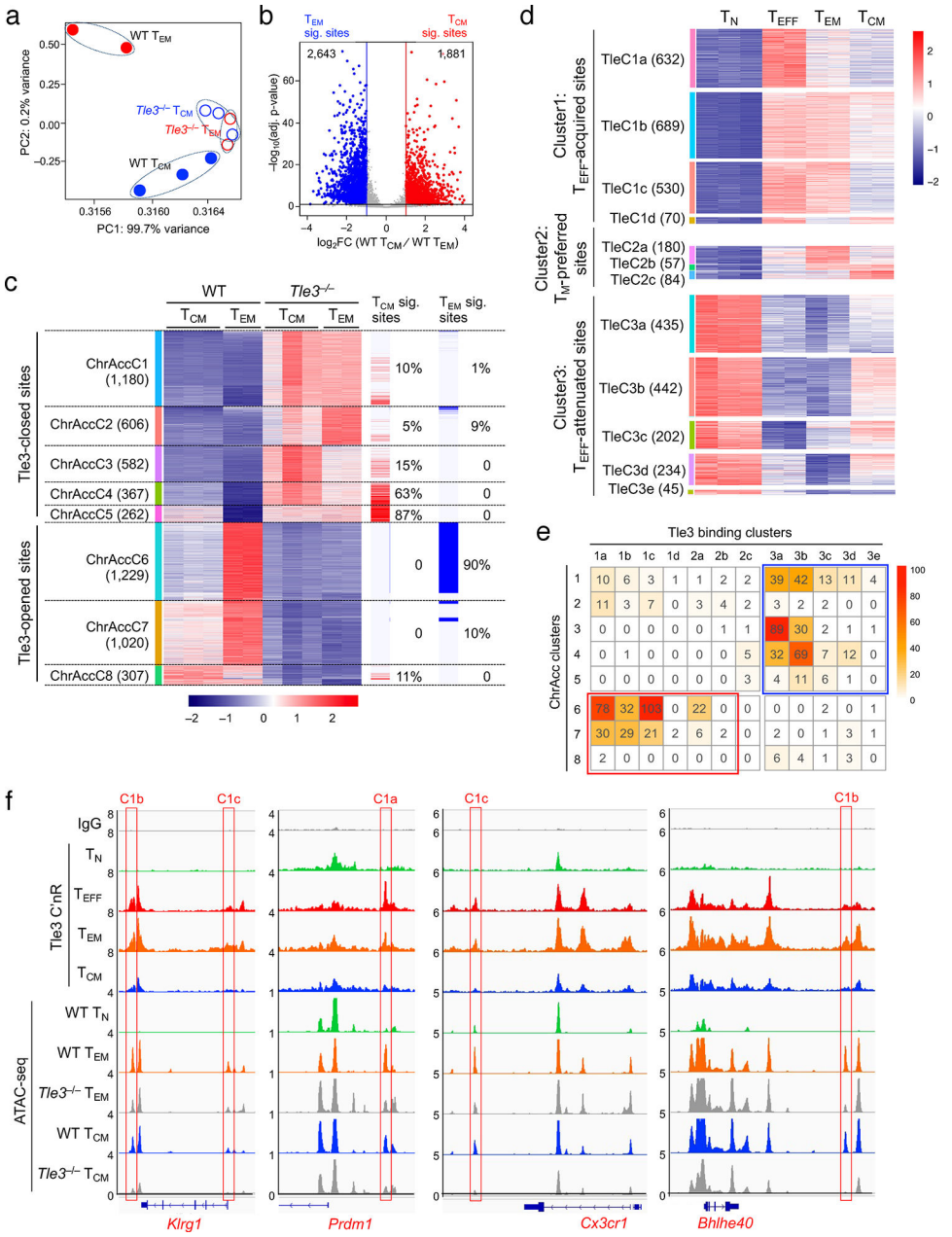

Figure 4. Tle3 promotes T_{EM}-characteristic open chromatin profile by acquiring novel binding sites.

a. Principal component analysis (PCA) of ATAC-seq libraries from WT and *Tle3*$^{-/-}$ T_{CM} and T_{EM} cells (≥30 *dpi*).

b. Volcano plot showing differential ChrAcc sites between WT T_{CM} and WT T_{EM} cells by the criteria of ≥2-fold expression changes and FDR<0.05. Values in the plot denote numbers of T_{CM} and T_{EM} signature ChrAcc sites.

c. Heatmap showing the impact of Tle3 deficiency on T_{CM} and T_{EM} ChrAcc landscape. Differential ChrAcc sites were identified in comparisons between WT and *Tle3*$^{-/-}$ T_{CM} and between WT and *Tle3*$^{-/-}$ T_{EM} cells, and distributed into 8 major ChrAcc clusters (ChrAccC) with K-means clustering analysis. Values in parentheses denote site numbers in each cluster,

and also marked are the overlapping rates of each cluster with T_{CM} and T_{EM} signature ChrAcc sites (defined in **b**), as indicated with red and blue lines, respectively.

d. Heatmaps showing three major Tle3 binding clusters and associated sub-clusters. Tle3 binding peaks were identified in T_N, T_{EFF}, T_{EM} and T_{CM} cells with CUT&RUN, and those with dynamic changes (≥ 3-fold change, FDR<0.05 in comparisons of T_{EFF}, T_{EM} and T_{CM} with T_N cells) were clustered based on Tle3 binding strength. Values in parentheses denote Tle3 peak numbers, and each row represents a Tle3 peak strength across different $CD8^+$ T cell response stages after Z-score normalization, with all replicates shown.

e. Correlation between ChrAcc and dynamic Tle3 binding changes. Diff. ChrAcc clusters (defined in **c**) were stratified against dynamic Tle3 binding clusters (defined in **d**), and the numbers of overlapping sites were indicated in each element.

f. Sequencing tracks of Tle3 binding (upper panels) and ChrAcc states (lower panels) at T_{EM}-characteristic genes as displayed on IGV. Open bars denote "T_{EFF}-acquired" Tle3 binding peaks and Tle3-opened ChrAcc sites, with Tle3 binding subcluster information marked on the top.

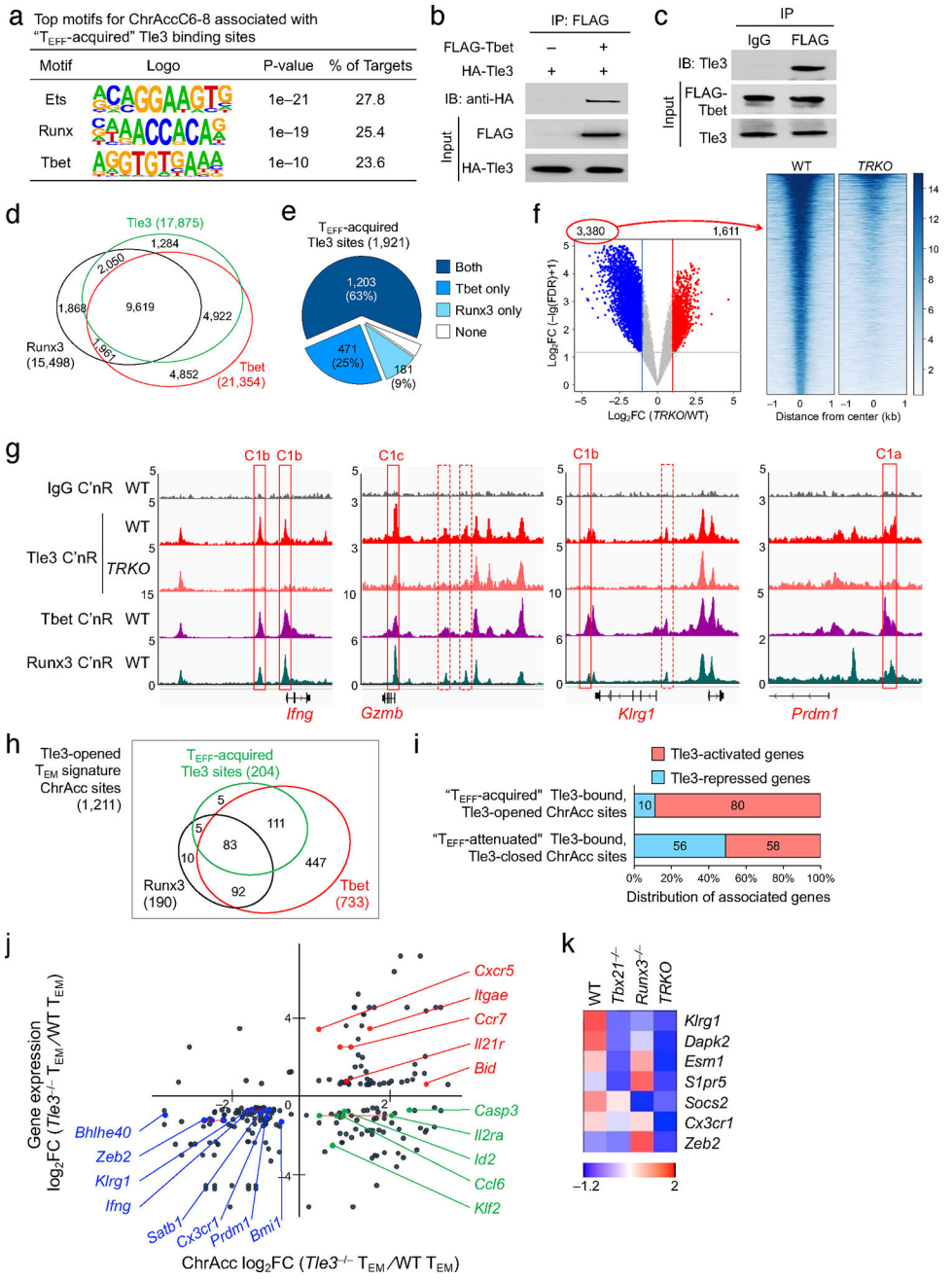

Figure 5. Tle3 functions as a coactivator of Tbet to positively regulate T_{EM}-characteristic molecular features.

a. *De novo* motif analysis of ChrAcc clusters 6–8 that overlapped with "T_{EFF}-acquired" Tle3 binding sites (within red rectangle in Fig. 4e).

b. Coimmunoprecipitation of FLAG-tagged Tbet and HA-tagged Tle3 after co-transfection into 293T cells. IP, immunoprecipitation; IB, immunoblotting.

c. Coimmunoprecipitation of FLAG-tagged Tbet with endogenous Tle3 in primary T_{EFF} cells (6 *dpi*) expressing retrovirally delivered FLAG-Tbet. Data in **b** and **c** are representative from two independent experiments.

d. Venn diagram showing overlap of Tle3 binding sites with Runx3 and Tbet binding sites in effector $CD8^+$ T cells as determined with CUT&RUN.

e. Pie chart showing overlapping rates of "T_{EFF}-acquired" Tle3 binding sites (TleC1a-d in Fig. 4d) with Tbet and Runx3 in effector $CD8^+$ T cells.

f. Volcano plot (left) showing differential Tle3 binding sites between WT and *TRKO* early T_{EFF} cells isolated on 4 *dpi*, with values denoting site numbers. Tle3 binding strength of the Tbet/Runx3-dependent Tle3 binding sites in WT and *TRKO* cells is shown in heatmap (right).

g. Sequencing tracks of Tle3 binding in WT and *TRKO* T_{EFF}, Tbet and Runx3 binding in WT T_{EFF} cells at T_{EM}-characteristic genes as displayed on IGV. IgG CUT&RUN (C'nR) in WT, Tbet C'nR in Tbet-deficient, Runx C'nR in Runx3-deficient T_{EFF} cells were performed as negative controls with similar sequencing output (the latter two tracks not shown for clarity). Open bars mark Tbet/Runx3-dependent Tle3 binding sites, where bars with solid lines denote overlap with "T_{EFF}-acquired" Tle3 binding peaks, with Tle3 binding subcluster information marked on the top.

h. Venn diagram showing overlap of Tle3, Tbet and Runx3 binding sites at Tle3-opened T_{EM} signature ChrAcc sites (from ChrAccC6–8 with blue bars in Fig. 4c).

i. Association of dynamic Tle3-bound, Tle3-opened and -closed ChrAcc sites (defined in Fig. 4e) with Tle3-activated and -repressed genes (defined in Fig. 3c).

j. Scatterplot showing the connection of dynamic Tle3-bound, Diff. ChrAcc sites with DEGs between WT and *Tle3*$^{-/-}$ T_{EM} cells, with select genes marked. Genes such as *Ccr7*, *Zeb2* and *Il2ra* are associated with multiple qualified ChrAcc sites, which are connected with red dotted lines.

k. Heatmap showing the impact of deficiency in Tbet and/or Runx3 on the expression of Tle3-activated T_{EM} signature genes. WT, *Tbx21*$^{-/-}$, *Runx3*$^{-/-}$ and *TRKO* P14 cells were adoptively transferred, and the recipients were infected with LCMV-Arm. On 4 *dpi*, early T_{EFF} cells were analyzed with RNA-seq, and the expression of select Tle3-dependent T_{EM} signature genes was displayed.

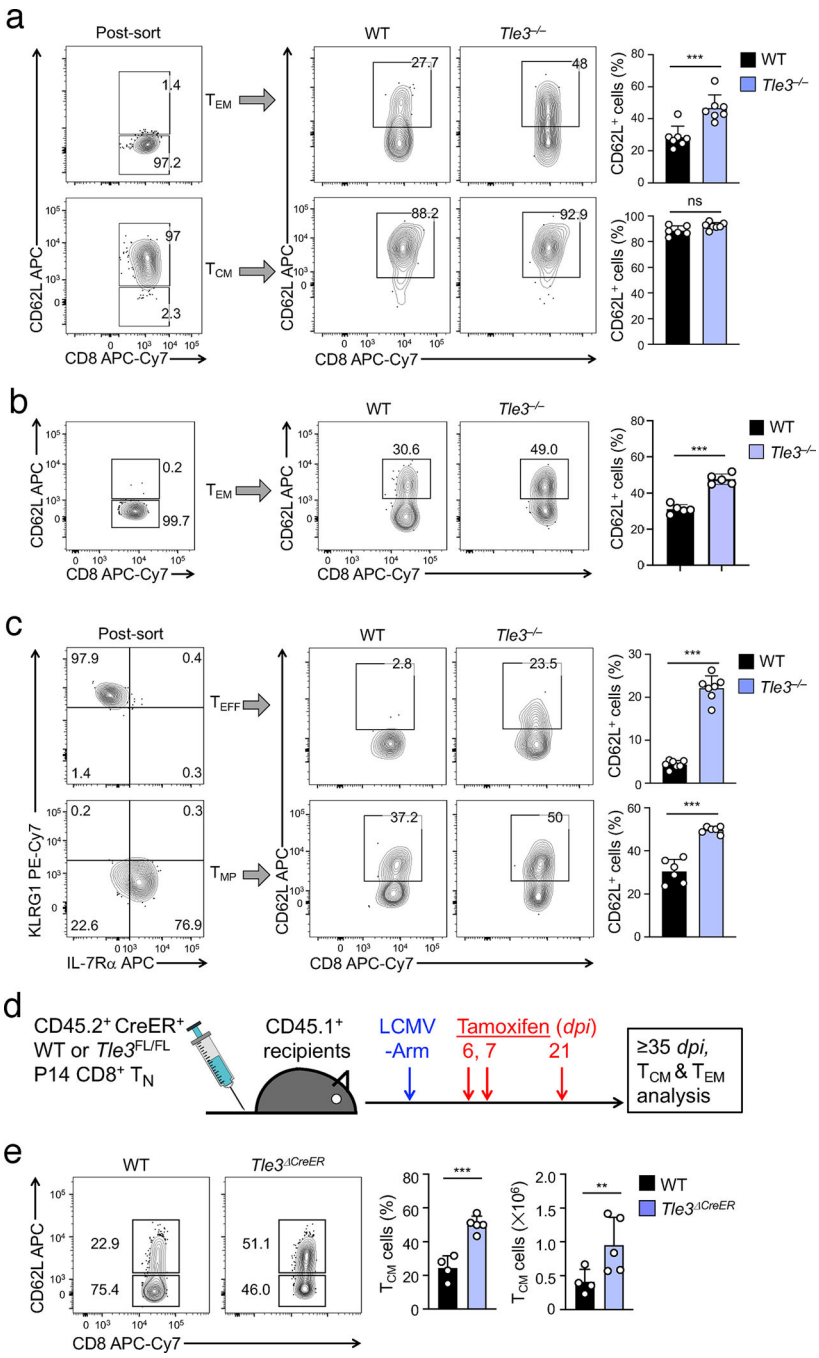

Figure 6. Lineage tracing reveals Tle3 deficiency promotes T_{CM} cell formation at all response stages.

a–b. Tle3-deficient T_{EM} cells are actively converted to T_{CM} cells. In *Gzmb*-Cre-mediated *Tle3* ablation (Fig. 1), T_{CM} and T_{EM} cells were sort-purified on 14 *dpi* (**a**) or ≥30 *dpi* (**b**) (left columns) and adoptively transferred into infection-matched CD45-disparate recipients (3×10^5 T_{CM} or 5×10^5 T_{EM} cells/recipient), followed by detection of $CD62L^+$ T_{CM} cells after 20 days (right columns).

c. Tle3-deficient T_{EFF} cells give rise to T_{CM} cells. In *Gzmb*-Cre-mediated *Tle3* ablation (Fig. 1), T_{EFF} and T_{MP} cells were sort-purified on 8 *dpi* (left columns) and adoptively transferred into infection-matched CD45-disparate recipients (1.5×10^6 T_{EFF} and 3×10^5 T_{MP} cells/recipients), followed by detection of $CD62L^+$ T_{CM} cells after 15 days (right two columns).

d. Experimental design for assessing the impact of induced *Tle3* ablation, where $CreER^+$ *Tle3*$^{+/+}$ and $CreER^+$ *Tle3*$^{FL/FL}$ P14 cells were used as donor cells (5×10^4 cells/recipient). The recipients were treated with Tamoxifen on 6 and 7 *dpi* to achieve Tle3 ablation at the effector phase, and treated again on 21 *dpi* to sustain Tle3 deletion.

e. Detection of T_{CM} cells in recipient spleens at ≥28 days after induced Tle3 deletion at the effector phase. All contour plots are representative data from ≥2 experiments, and cumulative data on T_{CM} cell frequency and numbers are means ± s.d. **, $p<0.01$; ***, $p<0.001$ by Student's *t*-test.

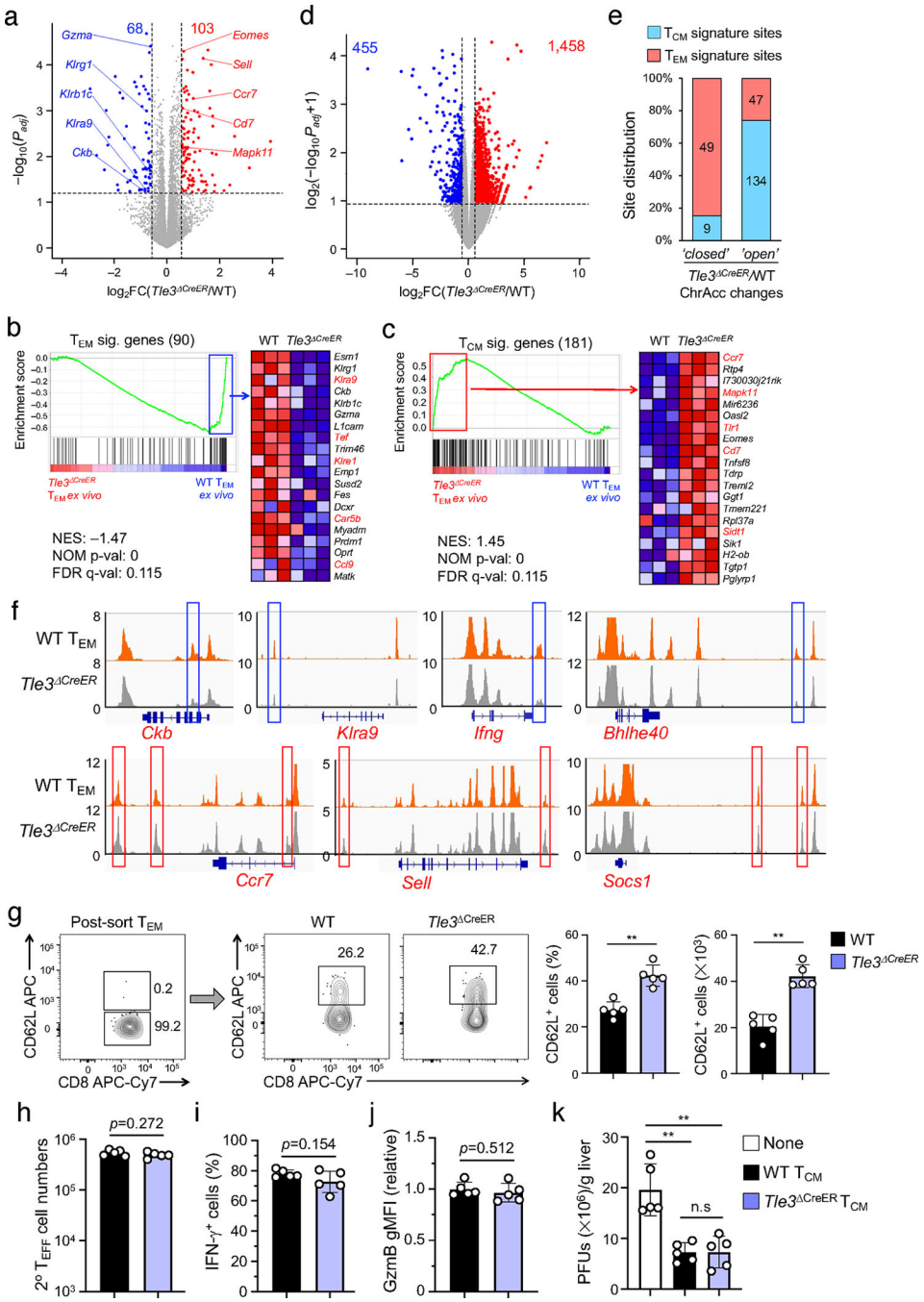

Figure 7. Induced *Tle3* deletion in 'established' T_{EM} cells promotes T_{CM} formation while sustaining its functionality.

a. Volcano plot showing DEGs between WT and *Tle3*$^{\Delta CreER}$ T_{EM} cells after *ex vivo* treatment with 4-OHT for 48 hrs, by the criteria of ≥1.5-fold expression changes and FDR<0.05. Values denote DEG numbers, and selected differentially expressed T_{CM} and T_{EM} signature genes are marked in red and blue, respectively.

b–c. Enrichment plots of T_{EM} (**b**) and T_{CM} (**c**) signature gene sets (defined in Fig. 3b) in comparison of *Tle3*$^{\Delta CreER}$ vs. WT T_{EM} cell transcriptomes with GSEA. In **b**, 37 of 90 T_{EM}

signature genes are in the leading-edge showing enrichment in WT T_{EM} cells. In **c**, 82 of 181 T_{CM} signature genes are in the leading edge showing enrichment in *Tle3*$^{\Delta CreER}$ T_{EM} cells. Top 20 enriched genes are shown in heatmaps for each gene set, with those in red denoting overlap with corresponding top 20 enriched genes in Fig. 3d and 3e, respectively.

d. Volcano plot showing differential ChrAcc sites between WT and *Tle3*$^{\Delta CreER}$ T_{EM} cells after *ex vivo* treatment with 4-OHT for 48 hrs, by the criteria of ≥1.5-fold ChrAcc changes and FDR<0.05, with values denoting site numbers.

e. Distribution of T_{CM} and T_{EM} signature ChrAcc sites in overlapping differential ChrAcc sites in *Tle3*$^{\Delta CreER}$ *vs.* WT T_{EM} cell comparison, with values in the plot denoting site numbers.

f. ChrAcc tracks at the T_{EM}- (top) and T_{CM}-characteristic genes (bottom) in WT and *Tle3*$^{\Delta CreER}$ T_{EM} cells. Blue open bars denote more 'closed' sites, and red bars denote more 'open' sites in *Tle3*$^{\Delta CreER}$ compared to WT T_{EM} cells.

g. Acute deletion of Tle3 in 'established' T_{EM} cells promotes generation of T_{CM} cells. WT and *Tle3*$^{\Delta CreER}$ T_{EM} cells were sort-purified from immune mice at 48 hrs after initial tamoxifen treatment and transferred into new hosts (5×10^5 T_{EM} cells/recipient), followed by detection of $CD62L^+$ T_{CM} cells after 14 days.

h–k. Recall capacity is sustained in Tle3-deficient T_{CM} cells. WT and *Tle3*$^{\Delta CreER}$ T_{CM} cells were sort-purified from immune mice at 14 days after initial tamoxifen treatment and transferred into *Rag1*$^{-/-}$ recipients (2×10^4 T_{CM} cells/recipient), followed by LM-GP33 infection. Three days after infection, the recipient spleens were harvested for analyses of T_{CM}-derived secondary (2°) effectors, including cell numbers (**h**), IFN-γ-producing fraction (**i**), and granzyme B expression (**j**). Also analyzed were recipient livers for colony-forming units (CFUs, **k**). Data are representative from one of two independent experiments.